


## Multi-scale and multi-parametric analysis of Late Quaternary event deposits within the active Corinth Rift (Greece)

GINO DE GELDER<sup>\*†‡</sup> , MAI LINH DOAN<sup>†</sup>, CHRISTIAN BECK<sup>†</sup>, JULIE CARLUT<sup>\*</sup>, CHLOÉ SEIBERT<sup>\*</sup>, NATHALIE FEUILLET<sup>\*</sup>, GARETH D. O. CARTER<sup>§</sup>, SOFIA PECHLIVANIDOU<sup>¶</sup> and ROBERT L. GAWTHORPE<sup>¶</sup>

<sup>\*</sup>Université de Paris, Institut de Physique du Globe de Paris, CNRS UMR 7154, Paris, 75005, France (E-mail: ginodegelder@gmail.com)

<sup>†</sup>ISTerre, CNRS, Université Grenoble Alpes, Université Savoie Mont Blanc, 1381 rue de la Piscine, Grenoble, 38000, France

<sup>‡</sup>Research Centre for Geotechnology, Research Organisation of Earth Science, BRIN, Komplek LIPI Gd. 70-80 Jl Sangkuriang, Bandung, 40135, Indonesia

<sup>§</sup>British Geological Survey, The Lyell Centre, Research Avenue South, Edinburgh, EH14 4AP, UK

<sup>¶</sup>Department of Earth Science, University of Bergen, Bergen, 5020, Norway

Associate Editor – Adam McArthur

### ABSTRACT

A major challenge in subaqueous palaeoseismology is to understand the relationship between an earthquake/tsunami and a sedimentary event deposit recorded in drillcores. Expedition 381 of the International Ocean Discovery Program was dedicated to understanding the development of the Corinth Rift, Greece. Its drilled cores provide a potentially important resource to better understand depositional mechanisms of sedimentary event deposits within changing open marine to (semi-)isolated environments. To achieve this, U-channels and spatula samples were analysed from the topmost part (0–65 m below seafloor maximum depth) of holes M0078B and M0079A (*ca* 0–25 ka), using high-resolution X-ray microtomography in combination with grain-size, magnetic and X-ray fluorescence measurements. Structures and grain fabric are resolved down to 10  $\mu\text{m}$  in voxel size, characterizing the geometry of the basal surface of ‘turbidite+homogenite’ sedimentary event deposits, and the internal base-upward evolution at high-resolution scale. This analysis suggests that these types of deposits are more complex than previously proposed, especially at the transition between the basal coarse turbidite sub-unit and the fine-grained homogenite upper sub-unit, as well as within the homogenite. Combined with the other observations and parameters, X-ray microtomography results are consistent with the interpretation of the Corinth ‘turbidite+homogenite’ deposits as having predominantly originated from seismic and/or aseismic slope failures followed by tsunami/seiche effects, despite subtle differences according to depositional environment.

**Keywords** Corinth Rift, gravity reworking, homogenites, IODP Expedition 381, microtomography, turbidites.

### INTRODUCTION

Over previous decades, the discipline of ‘subaqueous palaeoseismology’ developed with the aim of contributing efficiently to earthquake hazard

assessment (McCalpin, 2009). This approach needs to build on a tripartite relationship between: (i) a sedimentary event deposit; (ii) an earthquake with or without an associated tsunami wave; and (iii) an identified active fault, with possibly a known

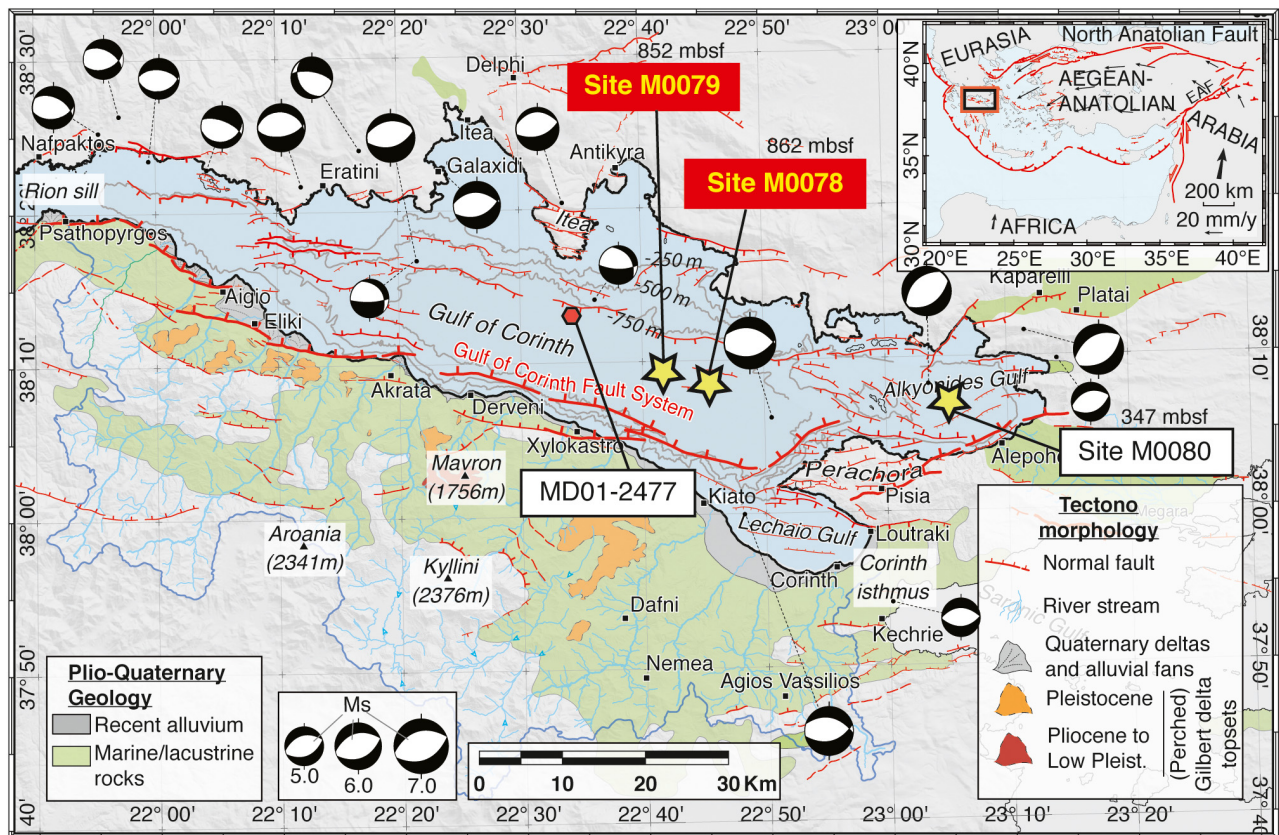


**Fig. 1.** Location of studied coring sites in the Gulf of Corinth. Stars indicate IODP-381 coring sites, with samples from red sites used in this study. Bathymetry is shown with contours every 250 m, and faults are the major onshore and offshore active faults bounding the Corinth Rift. Fault thickness indicates relative fault importance, and inset shows tectonic setting. After Fernandez-Blanco *et al.* (2019a) and references therein.

rupture location. These elements have been analysed, event-by-event, for sedimentary records (either marine or lacustrine) that span as much as tens of thousands of years (Marco & Agnon, 1995; Rodriguez-Pascua *et al.*, 2000), with correlations established between several different sites (McHugh *et al.*, 2006; Goldfinger *et al.*, 2007; Gràcia *et al.*, 2010; Polonia *et al.*, 2013, 2017; Ratzov *et al.*, 2015). Establishing relationships between element (3) and the two other elements, requires precise knowledge of a fault system's activity, and of the sedimentary fill adjacent to the fault (McHugh *et al.*, 2014; Beck *et al.*, 2012, 2015; Vanneste *et al.*, 2018; Van Daele *et al.*, 2019).

This study focuses on the relationship between elements (1) and (2), to understand better how sedimentary event deposits may be linked to earthquakes and/or tsunami waves. To achieve this, this work benefits from the recent drilling and coring surveys conducted in the active Corinth Rift (Greece), within the framework provided

by the 2017 International Ocean Discovery Program (IODP) Expedition 381 (McNeill *et al.*, 2019a,b; Fig. 1). During this expedition, three primary holes were drilled at three sites (Fig. 1). Borehole M0078A reached a depth of 610.43 metres below seafloor (m b.s.f.) in water depths of *ca* 860 m below sea level (m b.s.l.), borehole M0079A terminated at 704.9 m b.s.f. in water depths of *ca* 857 m b.s.l., and borehole M0080A penetrated to 534.1 m b.s.f. in water depths of *ca* 349 m b.s.l. An additional short hole was drilled at Site M0078, located approximately 20 m south of borehole M0078A, in order to better capture the sediment–water interface and shallow subsurface stratigraphy. This borehole, M0078B, recovered sediments to a depth of 55.85 m b.s.f.

The Corinth Rift benefits from a large amount of onshore and offshore surveys and monitoring (seismology, GPS kinematics, drilling, geophysical imagery and numerical modelling) (Armijo *et al.*, 1996; Rigo *et al.*, 1996; Briole *et al.*, 2000; Collier *et al.*,

2000; Cornet *et al.*, 2004; Pantosti *et al.*, 2004; Koukouvelas *et al.*, 2005; Leeder *et al.*, 2005; Bernard *et al.*, 2006; McNeill *et al.*, 2007; Bell *et al.*, 2009, 2011; Jolivet *et al.*, 2010; Taylor *et al.*, 2011; Pérouse *et al.*, 2012; De Gelder *et al.*, 2019; Fernández-Blanco *et al.*, 2019a,b; Pechlivanidou *et al.*, 2019). These investigations are dedicated to both surface impacts of active tectonics and crustal scale fault-mechanics. Offshore surveys focused on sedimentary reworking phenomena and their possible relationships with active tectonics and seismicity (Ferentinos *et al.*, 1988; Papatheodorou & Ferentinos, 1997; Papadopoulos, 2003; Lemeille *et al.*, 2004; Moretti *et al.*, 2004; Stefatos *et al.*, 2006; Campos *et al.*, 2013a; Campos, 2014; Beckers *et al.*, 2017, 2018). Initial development of the Corinth Rift started *ca* 5 Ma (Gawthorpe *et al.*, 2018), with the modern Corinth Rift forming around 0.6 to 2.0 Ma (Nixon *et al.*, 2016; Gawthorpe *et al.*, 2018; Fernandez-Blanco *et al.*, 2019a). The modern Corinth Rift is essentially a half-graben, with its active bounding faults near the southern margin (Corinth Rift Fault System; Fig. 1). Historical records include *ca* 100 > 5.5 Ms earthquakes in the Corinth Rift over the past *ca* 2500 years (Papazachos *et al.*, 2000), with instrumentally recorded earthquakes mostly located in the western and eastern sections of the rift (focal mechanisms in Fig. 1). Comparison of event deposits and historical earthquakes in the western rift suggest that the basin floor provides the highest potential to record imprints of earthquakes/tsunamis in its sediments, although also non-earthquake triggered landslides may result in sedimentary event deposits (Beckers *et al.*, 2017). The historical palaeotsunami record also dates back *ca* 2500 years (Papadopoulos, 2000), and includes tsunamis from both seismically and non-seismically induced landslides (e.g. Galanopoulos *et al.*, 1964). Several studies have focused on the sedimentary tsunami record in coastal areas (Kon-topoulos & Avramidis, 2003; Kortekaas *et al.*, 2011; Vött *et al.*, 2018), but it was also proposed that tsunamis/seiche waves are (partly) responsible for sedimentary event deposits on the Central Basin floor (Campos *et al.*, 2013a; Beckers *et al.*, 2017).

Effects of Late Quaternary climatic cycles on the bounding topographic relief also impacted the rift sedimentary infilling (Pallikarakis *et al.*, 2019; Watkins *et al.*, 2019). The offshore stratigraphy is strongly influenced by the sills at the western tip of the Gulf of Corinth (Rion sill: *ca* 60 m b.s.l., Fig. 1; and the *ca* 50–55 m b.s.l. Acheloos-Cape Pappas sill further west). Quaternary relative sea-level changes on the order of *ca* 120 m (De Gelder *et al.*, 2020) resulted in marine conditions during

interglacial periods like the Holocene, and (semi-) isolated (SI) conditions, resembling a lacustrine setting, during glacial periods (McNeill *et al.*, 2019b). As seismic reflection profiles image the lowstand of the last glacial *ca* 70 m below the present sea-level (Collier *et al.*, 2000), the water depth in the Central Basin floor, where the IODP-381 cores were drilled, varied between *ca* 860 m and *ca* 790 m over the past *ca* 25 ka. In terms of sedimentation, comparison between marine phases of deposition (for example, interval *ca* 13 ka–present) and (semi-)isolated (SI) phases of deposition (for example, interval *ca* 70–13 ka) indicate that sedimentation rates are generally lower, and bioturbation and organic carbon concentration higher, during marine intervals (Campos *et al.*, 2013a; McNeill *et al.*, 2019a,b).

Previous studies on sediments cored within the Corinth Rift infill, documented the interlayering of numerous ‘event deposits’ – rapidly deposited layers related to earthquakes, tsunamis/seiches, (subaqueous) landslides and/or river floods – within a fine-grained hemipelagic slow and continuously deposited background sedimentation, both during marine and SI episodes (Campos *et al.*, 2013a; Campos, 2014). These event deposits are generally composed of a coarse basal sub-unit and a fine-grained upper one, and often described as ‘turbidites’. Nevertheless, they are not necessarily related to gravity reworking, and a wide range of origins, and of single *versus* complex depositional mechanisms, has to be considered. To better constrain the origins and mechanisms of these sedimentary event deposits in the Corinth Rift, and check the possible influence of the environment, the last marine/SI alternation was investigated (*ca* 25 ka; Fig. 2); particular focus was on the limit between coarse basal and upper fine-grained sub-units, and used a multi-parametric approach including high-resolution X-ray tomography, in combination with grain-size, magnetic and XRF measurements.

## DATA ACQUISITION AND PROCESSING

Observations and measurements discussed in this section are based on: (i) part of the observations and analyses performed by the whole IODP Expedition 381 science team in the MARUM (University of Bremen) during the Onshore Science Party (OSP; February 2018; McNeill *et al.*, 2019a); and (ii) processing of specific selected post-cruise samples (Fig. 2). Specifically, eight U-channels were sampled from the cores of Holes M0078B and M0079A located at

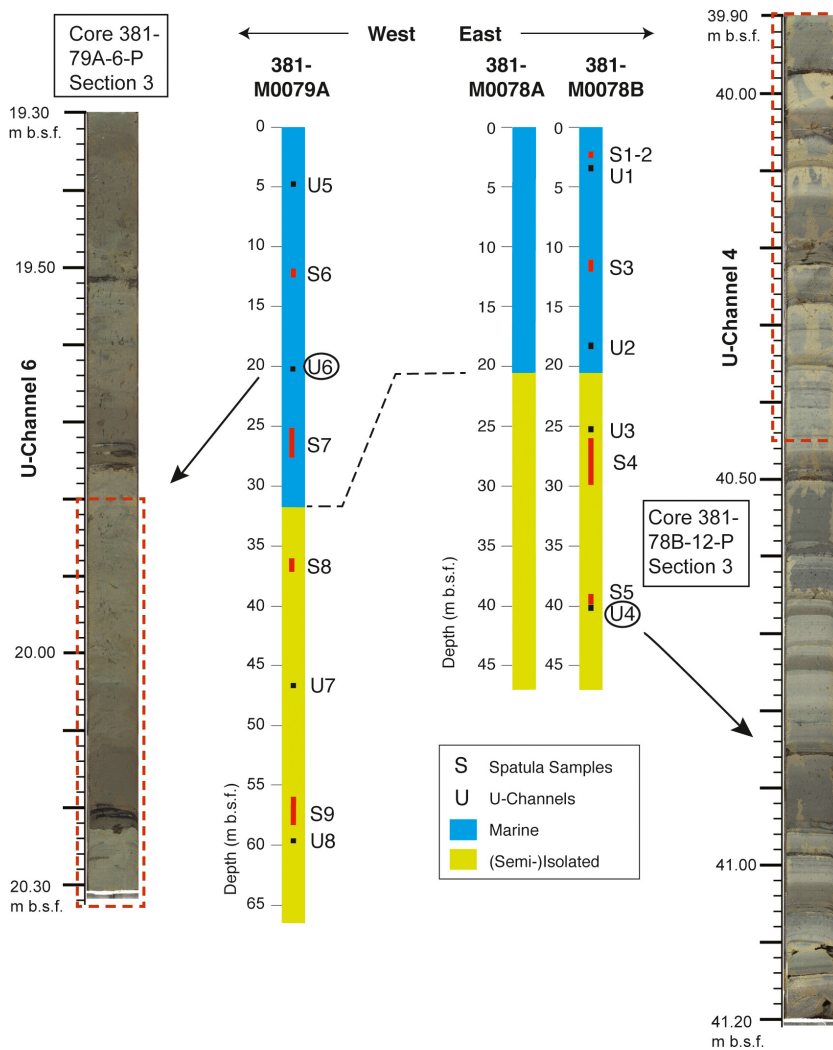


**Fig. 2.** Location of different sampling within the last *ca* 25 ka interval. View of split core sections that are presented in detail within the manuscript (Figs 6 and 7). Red dashed rectangles indicate the exact U-channel positions.

sites M0078 and M0079, respectively (Fig. 1) and eight intervals with spatula samples, half from the most recent marine interval (*ca* 13–0 ka) and half from the upper portion of the most recent SI interval (*ca* 25–13 ka). In total, these samples comprise eight event deposits from the marine interval, and ten from the SI interval.

The results are illustrated and described using representative U-Channels 4 and 6 (Fig. 2), with results from the other U-channels and spatula samples presented in the Appendix S1. Preliminary results of the whole OSP and raw data of IODP Expedition 381 (Expedition Report) are accessible on <http://www.ecord.org/expedition381/>.

## Non-destructive analyses

### *Volume magnetic susceptibility*

To constrain magnetic susceptibility (MS) within sedimentary event deposits two sets of

measurements were used: (i) part of the initial IODP MSCL GEOTEK™ core logging data (MARUM, University of Bremen; Geotek Limited, Daventry, UK) recorded on the whole cores at 2 cm resolution; and (ii) 0.5 cm resolution measurements made on U-channels using a BARTINGTON™ MS2 contact sensor (ISTerre Laboratory, Savoie-Mont-Blanc University; Bartington Instruments Limited, Witney, UK).

### *X-ray fluorescence*

To decipher the chemical composition of sedimentary event deposits, also in comparison to the hemipelagic ‘background’ sedimentation, two sets of X-ray fluorescence (XRF) measurements were used (AVAATEC™ device; Avaatech XRF Technology, Dodewaard, The Netherlands): (i) whole-core measurements with 5 mm spacing obtained using the XRF-scanner in MARUM (University of Bremen) on the intervals of the undisturbed half of the split



cores corresponding to all U-channels; and (ii) high resolution profiles (1 mm spacing) performed in EDYTEM Laboratory (Savoie-Mont-Blanc University) on four of the retrieved U-channels.

Because XRF analysis does not provide absolute chemical compositions, but relative activity of concerned elements, ratios of selected elements were used to characterize variations in sediment compositions, following Croudace *et al.* (2006). Twenty-four ratios were specifically selected from the overview of Rothwell & Croudace (2015) that may indicate changes in: (i) biogenic/detrital sedimentation; (ii) sedimentary provenance and grain size; (iii) productivity and post-depositional alteration; and (iv) organic content. As most of the source areas for the Gulf of Corinth deposits are carbonate dominated, Ca ratios need to be carefully interpreted. Principal Component Analysis (PCA) was applied to these ratios in order to determine: (i) the relative importance of different principal components to the overall variation in XRF values; and (ii) the specific XRF ratios responsible for most significant changes within a principal component (Fig. S1). This study shows only these most important elemental ratios within the *Results* section, i.e. those with the highest relative contributions to principal components.

#### *Anisotropy of magnetic susceptibility*

To measure anisotropy of magnetic susceptibility (AMS) within the U-channels juxtaposed, 2 cm-side, oriented cubes of sediments were extracted and measured using an AGICO™ MFK1-FA Kappabridge (automatic spinning, 64 orientations per sample; AGICO Inc., Brno, Czech Republic) at the Institut de Physique du Globe de Paris. Following the classification of Jelinek (1981) the following parameters were considered: foliation, lineation, shape parameter T, corrected anisotropy degree Pj, inclination of Kmin ellipsoid axis and the declination of Kmax ellipsoid axis.

#### *Two-dimensional X-ray images*

X-ray images of all U-channels were obtained in EPOC Laboratory (Bordeaux University) using the SCOPIX device and procedure (Migeon *et al.*, 1998).

#### *X-ray microtomography*

High-resolution three-dimensional X-ray imaging was performed on 2 cm-side, oriented cubes (as tests), and on 20 cm long portions of U-channels. An EASYTOM™ XL Nanofocus tomograph (RX Solutions, Plymouth, MN, USA) located in

Grenoble-Alpes University was used. The source is a tungsten filament producing a source beam of ca 3.5 µm in diameter. The receiver is a flat panel of 1840 × 1456 pixels. Helicoidal recording allowed scanning lengths up to 20 cm within a single acquisition in about 5 h. Reconstruction of the tomographic volume was done with RX-Solution's X-act software. This procedure permitted 3D imaging of radiodensity within the scanned volume at a 10 µm voxel size. In the latter analysis, intensity of grey in the image was used as a proxy of density, although it is noted that the radiodensity also depends on atomic number. Segmentation of resolved grains provided additional textural properties (grain-size distribution, grain shape and possible preferential orientations). Processing of the scanned images was performed twice with two independent software packages; ImageJ for thresholding and segmenting the grains and the Python scikit-image package for 3D reconstruction.

The high resolution of the microtomography at the 10 µm-scale allows a detailed characterization of event deposits, albeit only on portions of maximum 20 cm. Since X-ray micro-tomography data is sensitive to the density of the material, X-ray data were used in two different ways: (i) by getting a continuous recording of texture, averaging radiodensity along a selected band; and (ii) by digitally segmenting out the heavy grains embedded within the clayey matrix and characterization of their morphological properties. Heavy grains are segmented slice by slice through thresholding, and shape analysis was performed to retrieve their size, orientation and shape ratio. This analysis allows the authors to highlight the distribution of these grains with depth.

#### **Grain-size distribution**

Besides measurements dedicated to textural analysis of the grain fabric ('*Anisotropy of Magnetic Susceptibility (AMS)*', '*Two-dimensional X-ray images*' and '*X-ray microtomography*' sections), additional observations (optical microscopy) and grain-size measurements on individual samples were made.

Laser microgranulometry was performed using a MALVERN™ Sizer 2000 laser diffraction particle size analyser (Malvern Panalytical, Malvern, UK; at the ISTERre Laboratory, Savoie-Mont-Blanc University) on both: (i) individual 'spatula' samples selected during the IODP Leg 381 OSP (MARUM, University of Bremen), picked at variable spacing of 0.5 to 5.0 cm; and (ii) samples extracted from the U-channels at spacing of 0.5 to 2.0 cm.

## Chronological control

For the purpose of this study only an approximate chronology was required, for which the general chronostratigraphy deduced from correlation between core data and seismic reflection profiles was followed. Seismic stratigraphy is interpreted in the context of the current understanding of Late Quaternary sea-level fluctuations and their impact on the Gulf of Corinth. The investigated intervals of this study (Fig. 2) correspond to the last alternation of marine and (*semi-isolated*) environments. Previous radiocarbon dating and correlation with sea-level curves places the transition between those environments at *ca* 12 to 13 ka (e.g. McNeill *et al.*, 2019b). Assuming that sedimentation rates between this transition and the underlying marine sub-unit (*ca* 70 ka; McNeill *et al.*, 2019b) have been constant, the oldest U-channels herein are estimated to be around *ca* 25 ka.

## RESULTS

The results of detailed analyses of the U-channels and spatula samples are presented below. Note that additional results are presented as Appendix S1.

Sedimentary event deposits are referred to either as a classical turbidite (Tu) or a 'turbidite+homogenite' (TuHm). Figure 3 illustrates the two types of event deposits, particularly different in the nature of the transition between a coarse fining-upward lower unit (possibly multiple fining-upward sub-units) and a highly homogeneous fine-grained upper unit. The transitions between homogenites and their overlying hemipelagic intervals were defined based on texture (*Grain-size distributions* section) and XRF chemistry (*X-ray fluorescence* section); for several event deposits these transitions were also compared with X-ray 3D microtomography data (*X-ray micro-tomography data* section). The word 'homogenite' is used only in a descriptive sense: fine-grained layers, lacking visual layering or other features, and apparently sharply separated from a coarser sub-unit. No depositional mechanism is inferred; the interpretation is discussed based on our data and different published investigations in the *Discussion* section. The word 'turbidite' is also used in a descriptive sense. Although the term 'hemipelagite' usually concerns marine deposits, in this study it is applied for slowly accumulated background

sediments during both marine and '(semi-) isolated' (SI) environments. In the following 'sub-units' is used for the different parts within a turbidite (Tu) or a turbidite+homogenite (TuHm) event deposit.

## Layering and composition

The investigated core portions (down to 65 m b.s.f. in borehole M0079A) display a clear layering with alternating dark grey to whitish, essentially fine-grained sediments (silty clay/clayey silt). Minor coarser material (very fine sand to rare medium sand with a clayey-silty matrix) with higher siliclastic content is present along the whole succession. Individual layers are millimetres to tens of centimetres thick (*cf.* close-ups on Fig. 2), resulting from the intercalation of different types of event deposits within a fine-grained, layered 'background' sedimentation consisting of hemipelagic deposits. Fine-grained facies are calcareous muds in which the carbonate fraction is biogenic or detrital. In the marine interval primary biogenic components mostly consist of nanoplankton and rare planktonic foraminifera, whereas in the SI intervals it mostly consists of bio-induced calcite and diatoms. Detrital grains are mostly calcite for both intervals. The silt-size and clay-size clastic fraction comprises calcite, clay minerals, quartz and altered ferromagnesian debris. Aragonite needles also occur, especially in the transition between marine and SI units.

## Grain-size distributions of hemipelagites and homogenites

Given the small amount of samples of turbidites (<5% of all samples), this study only focuses on the fine-grained layers in this section and Fig. 4. Sampling for grain-size characterization of homogenites and hemipelagites was based on visual observations of the split cores from boreholes M0078B and M0079A. U-Channels 1, 2, 5 and 6 within the marine interval, and U-Channels 3, 4, 7 and 8 within the SI interval were selected. To characterize each homogenite or hemipelagite sample, the D50 (or median) and the D99 that represent the 'mean' grain-size and the coarsest grain-size fraction, respectively (Fig. 4A to D), and two grain analysis parameters, sorting and skewness, were used (Fig. 4E to H). The eight binary cross-plots of these two parameters shown in Fig. 4 allowed the authors to investigate: (i) possible differences between hemipelagites and homogenites;

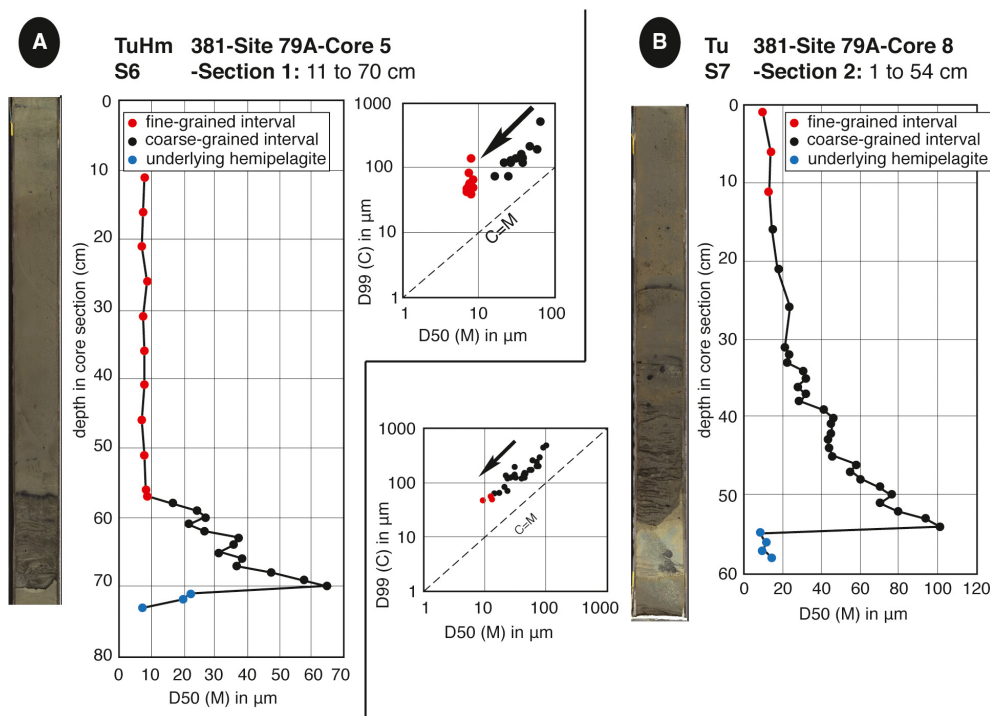


**Fig. 3.** Selected examples of a single turbidite+homogenite (TuHm; left) and a 'classical' turbidite (Tu; right). Base-to-top grain-size evolution is shown with D50 (Median or M), and Passega CM diagram (1964) combining the D50 (M) and the D99 (C) in logarithmic coordinates. Location of samples S6 and S7 is shown on Fig. 2.

and (ii) possible influence of the depositional environment (i.e. marine or SI) on both.

Figure 4A to D do not show significant differences neither between the two types of units nor between the two environments; in both cases, hemipelagite values appear slightly more dispersed. Regarding distribution parameters, sorting and skewness, all samples depict values between 0.8 and 1.2 for skewness and between 1.7 and 2.5 for sorting, except for a few samples of marine hemipelagites (Fig. 4E and G). There are both marine hemipelagite samples that display a very good sorting (<1.5), and samples that show a weak sorting (>2.5) and a highly asymmetrical distribution. Homogenites do not appear to be significantly different in marine or SI units. For both environments, homogenite samples appear slightly less dispersed than hemipelagites, and SI homogenites display a similar range of values for sorting and skewness with respect to SI hemipelagites (Fig. 4).

### X-ray fluorescence chemical analysis

Figure 5 summarizes results from all U-channels with separate distributions for hemipelagites,

homogenites and turbidites. Figure S2 shows additional XRF counts and Fig. S3 shows the 24 detailed XRF ratios of all U-channels as a function of depth. The following main characteristics are highlighted.

- In terms of biogenic/detrital origin (Fig. 5A and C), chosen XRF chemical parameters discriminate the three types of units. Turbidites and homogenites have relatively similar ratios, with the exception of Ca/Fe that is generally lower in homogenites. Homogenites have lower Ca ratios than hemipelagites (Ca/Fe, Ca/Ti and Ca/Sr), indicating a generally higher detrital content. The Ca/Sr ratio in SI conditions (Fig. 5C) is the only exception and, combined with the decrease in Ti/Sr ratios as well as the overall increase in Sr for the SI U-channels (Fig. S2), this suggests that the increased Sr during SI conditions affects hemipelagite composition more than turbidite and homogenite composition.
- In terms of organic content (Fig. 5B and D), turbidites, homogenites and hemipelagites have a similar range of values, with the main difference that hemipelagites appear to have a mostly bimodal distribution. The overall lower Br/Cl

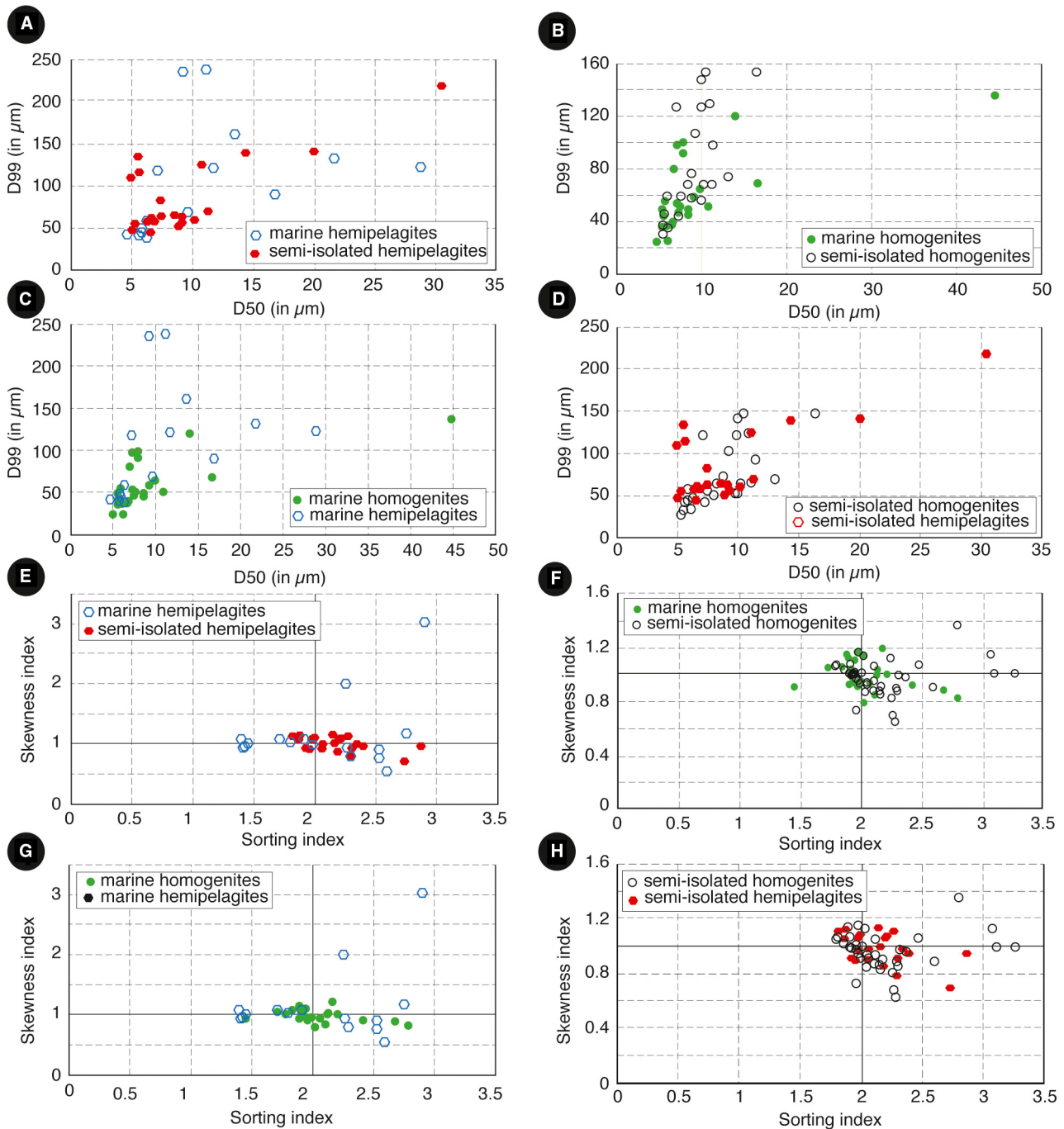


**Fig. 4.** Binary cross-plots of grain-size parameters of hemipelagites and homogenites in marine and (semi-)isolated (SI) environments. Marine samples from U-Channels 2, 5 and 6 (15 hemipelagite and 24 homogenite samples), SI samples from U-Channels 3, 4, 7 and 8 (22 hemipelagite and 35 homogenite samples). Diagrams (A) to (D) display a general characterization through D50 (Median) and D99 (coarsest particles). Diagrams (E) to (F) show depositional processes through classical Sorting and Skewness indices. Location of U-channels is shown on Fig. 2.

ratios during SI conditions is in line with the overall Br decrease (Fig. S2).

• In terms of sedimentary provenance/grain size (Fig. 5E and G), turbidites show a larger

variation with respect to homogenites and hemipelagites, which may be partly due to varied terrigenous sources and/or to larger grain size. Homogenites display a generally narrow range of



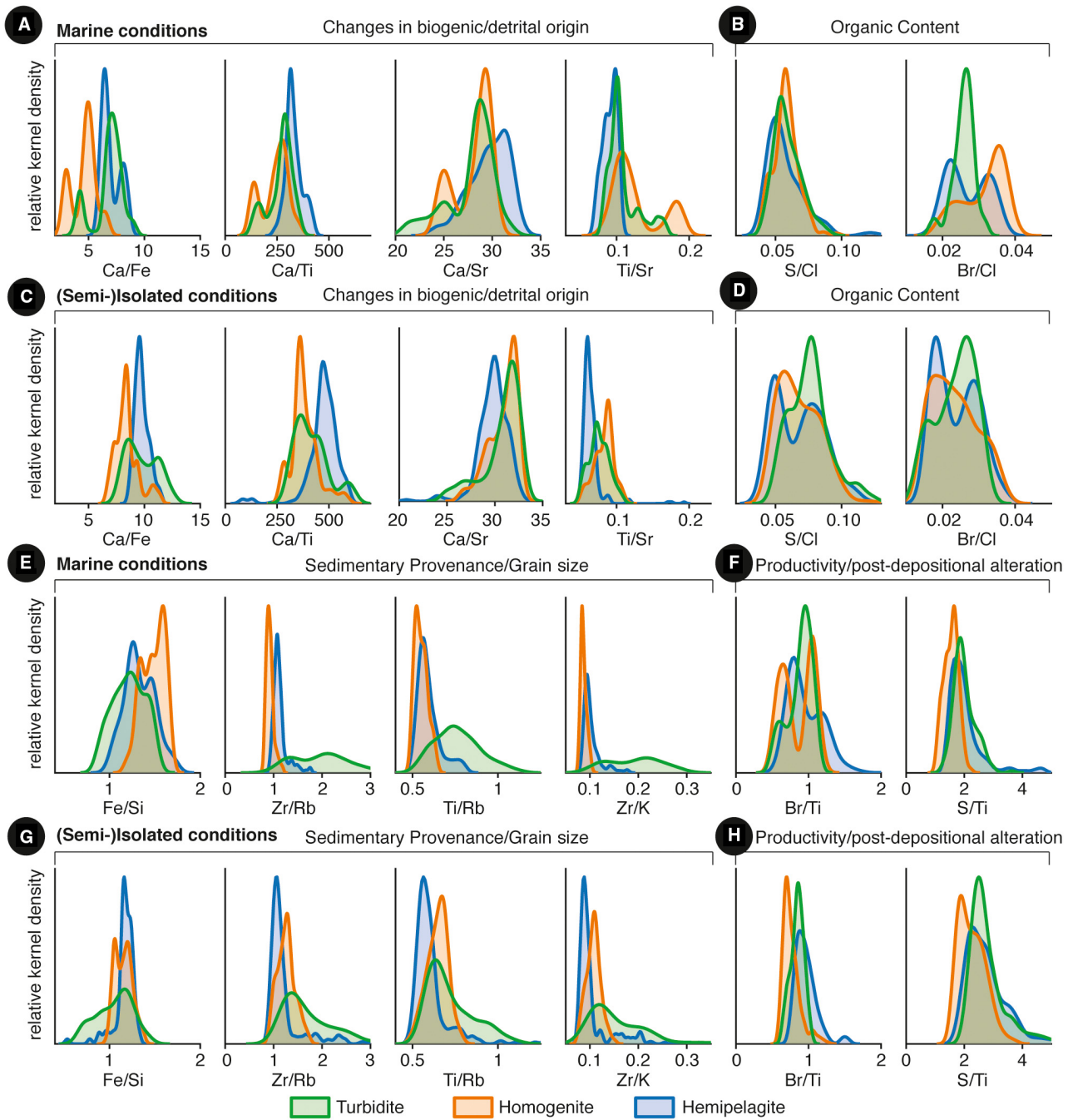


**Fig. 5.** X-ray fluorescence (XRF) ratios for marine versus (semi-)isolated (SI) conditions. Selection of 12 XRF ratios, distinguishing between Turbidites, homogenites and hemipelagites. Measurements come from all ten U-channels; values referred as ‘turbidites’ come from classical turbidites (single Tu) and coarse bases of turbidites+homogenites (Tu term of TuHm).

values, indicating chemical and mineralogical homogeneity with respect to hemipelagites, which generally have a skewed distribution. The authors note that peak values for Zr/Rb, Ti/Rb and Zr/K in homogenites are slightly lower than hemipelagite

peak values during marine conditions, but slightly higher during SI conditions. Given that homogenite values remain relatively constant, this suggests a slight change in the overall mineralogical composition of hemipelagites.

- In terms of productivity and post-depositional alteration (Fig. 5F and H), Br/Ti ratios appear slightly higher and more variable during marine conditions for all three types. Concerning S/Ti ratios, homogenites seem to have slightly lower values than those obtained for turbidites and hemipelagites.

Overall these observations show that turbidites, homogenites and hemipelagites have distinct chemical characteristics, and that there are some differences in chemical composition between marine and SI depositional environments, particularly within hemipelagites.

### Correlations of geochemical, magnetic and textural parameters

The XRF and textural parameters are presented for U-Channels 4 and 6 (Figs 6A, 6B and 7A, 7B, respectively); the same measurements applied to the other U-channels are available in Fig. S4, and detailed event deposit description in Table S1.

In U-Channel 4 (Fig. 6) five different sedimentary event deposits were observed. Event deposits 1 and 5 are classical turbidites (Tu), and event deposits 2, 3 and 4 are turbidite+homogenite deposits (TuHm). Grains are especially coarse for event deposits 2 and 5, with respective D50 values of 30  $\mu\text{m}$  and 50  $\mu\text{m}$ , which are also the thickest event deposits in this U-channel (5–10 cm). The peak in magnetic susceptibility at the top of event deposit 5 is at the same depth as a cluster of black grains, and thus probably related. AMS foliation is particularly high in the homogenites of event deposits 2 and 4, with the lineation overall low apart from a gradual increase within event deposit 5. In general, the Kmin inclination is close to vertical, indicating relatively flat-lying grains, and the Kmax declination is strongly variable, indicating no strong preferred orientation of grains in the horizontal plane. Looking at the XRF ratios, the Ca/Ti and Ca/Fe ratios are generally lower within sedimentary event deposits, and show sharp changes around transitions with hemipelagic intervals. Zr/Rb is particularly high in turbidites, sharply decreasing upward within TuHm event deposits 2 and 4, and a more gradual decrease within Tu event deposit 5. The separation between two homogenite intervals (Hm1 and Hm2) in event deposits 2 and 4 is particularly clear from core images and X-rays, and for event deposit 2 this sharp change is also expressed in changing Ca/Ti, Ca/Fe and Fe/Si ratios.

U-Channel 6 (Fig. 7) only contains one *ca* 19 cm thick sedimentary event deposit. All selected XRF ratios display highly variable values within the lower turbidite interval between 20.26 and 20.22 m b.s.f., and show similar trends as those of the grain-size variations. The top of the event deposit at 20.06 m b.s.f. is marked by a sharp shift of Ca/Ti, Ca/Fe, Ca/Si, Cu/Rb and Mn/Ti ratios (Fig. 7 and Fig. S4). The visually detected subdivision of the homogeneous mud interval, interpreted as Hm, is confirmed by slight changes of Ca/Ti, Ca/Fe, Ca/Si, Si/Ti, Fe/Rb and Fe/Ti (Hm1 and Hm2 in Fig. 7), similar to event deposit 4, but not to event deposit 2 in U-Channel 4 (Fig. 6). The volume magnetic susceptibility is low overall, but higher in the finer-grained intervals than in the coarse base. Magnetic susceptibility roughly follows the same trend as the Fe/Si ratio indicating a likely control of this parameter by the relative proportion of iron oxides. Whereas magnetic susceptibility is constant in Hm1, it shows slightly more variation in Hm2, possibly due to heterogeneities associated with larger grains.

The entire homogenite interval in U-Channel 6 (Fig. 7), displays a higher magnetic foliation with respect to the overlying hemipelagic layer and with respect to the coarse turbidite base. Shape parameter T (oblate ellipsoid distribution), lineation, Kmax declination and Kmin inclination (vertical) do not display clear changes between the different deposit types. When looking at the Hm interval in more detail, a change in magnetic foliation around the Hm1/Hm2 separation is noted. Grain-size distribution also underlines this contrast in the D99, but within suspended-load ranges.

### X-ray micro-tomography data

#### Quantitative measurements

Selected portions imaged through X-ray micro-tomography for U-Channels 4 and 6 are presented on Figs 6C, 6D and 7C, respectively, with correlation to the detailed XRF profiles. The same measurements applied to U-Channels 2 and 8 are available in Fig. S4. The averaged density is shown along a band highlighted with green shading, and the morphological properties of the suspended heavy grains with yellow patches (HR X-ray images in Figs 6 and 7).

The high porosity associated with the turbiditic base has a stronger effect on the density than the general occurrence of heavier grains, so that the turbiditic base generally has a lower

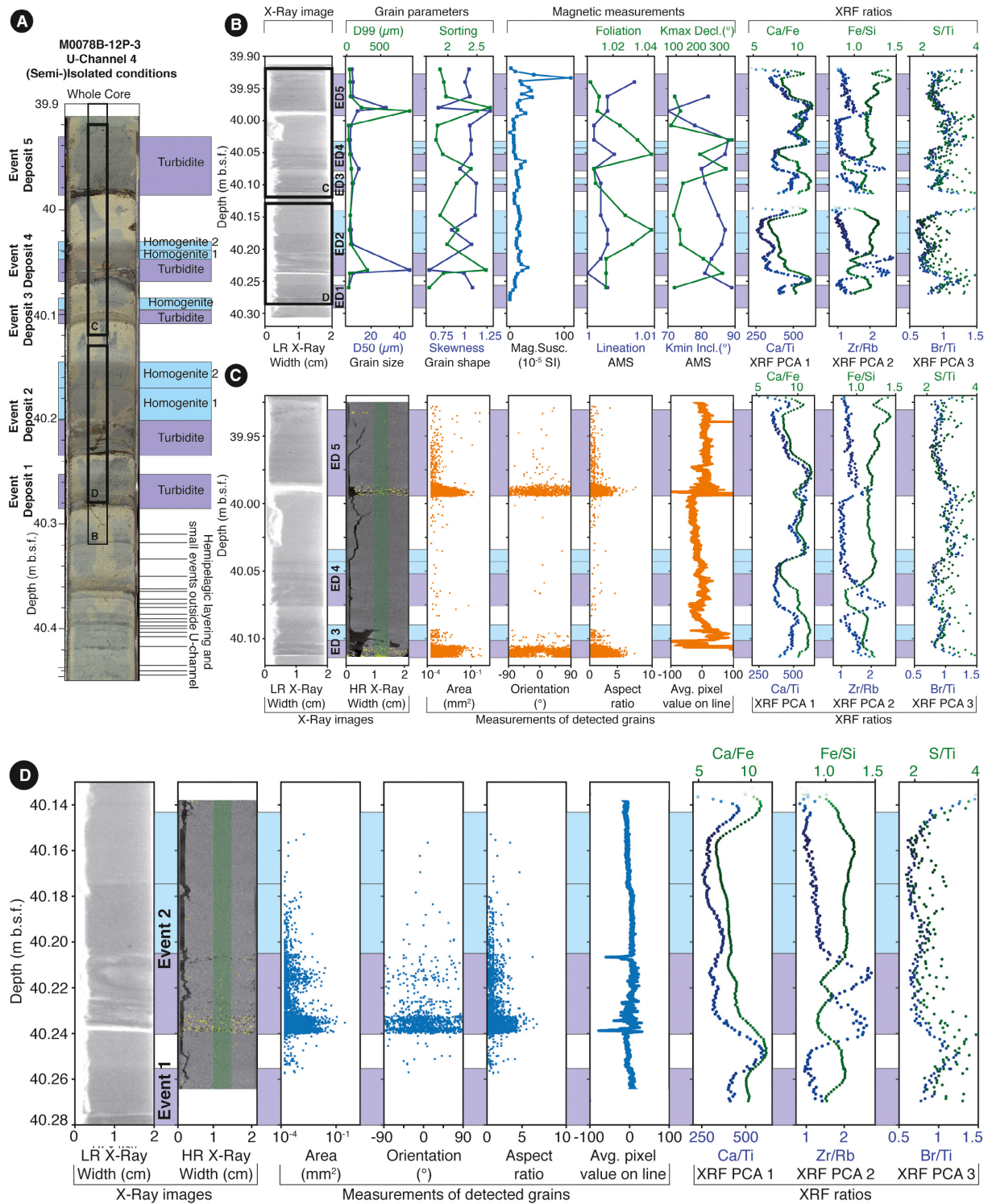


**Fig. 6.** Overview of U-Channel 4. (A) Whole core overview including position of U-channel and different event deposits. (B) Low Resolution (LR) X-ray image and measurements of U-Channel 4, including grain size, grain shape, magnetic susceptibility, Anisotropy of Magnetic Susceptibility (AMS) and selected X-ray fluorescence (XRF) ratios for each of the three strongest Principal Components (see Fig. 5). (C) Zoom-in on upper portion of U-Channel 4, including Low Resolution (LR) and High Resolution (HR) X-ray images and measurements of area, orientation, and aspect of visible grains in HR X-ray, average pixel value in HR X-ray, and the same XRF ratios as in (B). (D) Same as in (C), but for the lower portion of U-Channel 4.

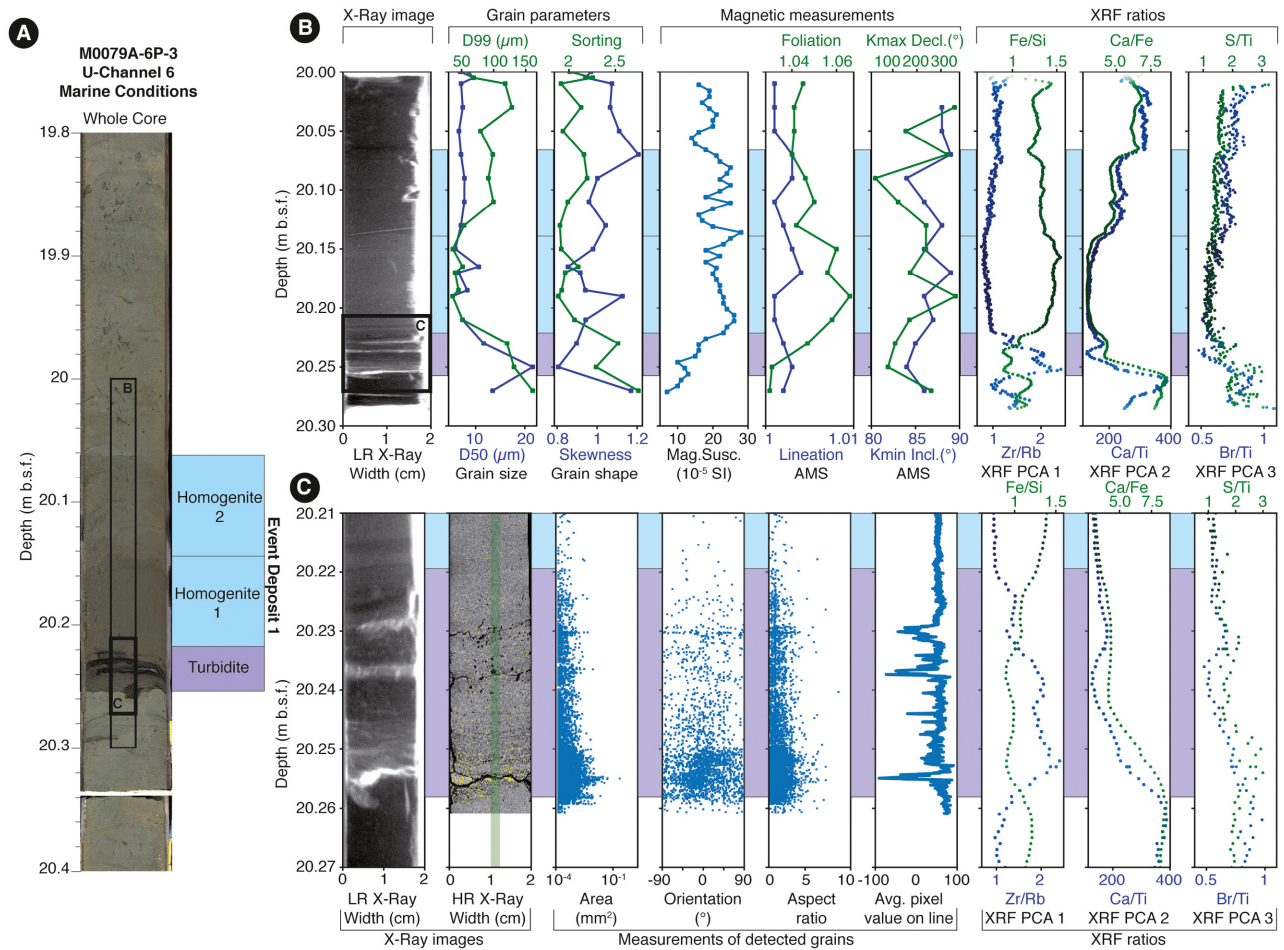


**Fig. 7.** Overview of U-Channel 6. (A) Whole core overview including position of U-Channel 6 and different event deposits. (B) Low Resolution (LR) X-ray image and measurements of U-Channel 6, including grain size, grain shape, magnetic susceptibility, Anisotropy of Magnetic Susceptibility (AMS) and selected X-ray fluorescence (XRF) ratios for each of the three strongest Principal Components (see Fig. 5). (C) Zoom-in on turbidite interval of U-Channel 6, including Low Resolution (LR) and High Resolution (HR) X-ray images and measurements of area, orientation, and aspect of visible grains in HR X-ray, average pixel value in HR X-ray, and the same XRF ratios as in (B).

density (average pixel value, Figs 6 and 7) than the underlying hemipelagite. The exception is event deposit 5 in U-Channel 4 in which the entire turbidite interval has a higher density than the underlying hemipelagite. Both homogenite profiles with separate Hm1/Hm2 intervals (event deposits 2 and 4, Fig. 6) have a small offset in density between a slightly heavier Hm1 and lighter Hm2. Also, in U-Channel 4 (event deposit 2, Fig. 6D), heavy grains are clearly scarcer above this transition. In the U-Channel 6 event deposit, the base of Hm1 (Fig. 7c) displays faint fluctuation in grey scale.

Figure 6C shows the occurrence and size of heavy grains (see *X-ray micro-tomography*

section) within event deposit 5, fining-up gradually, as expected from a dilute turbidite deposit. Similarly, Fig. 6D reveals three clear sub-units of coarser laminations with heavy grains at the turbiditic base of event deposit 2 (40.24, 40.235 and 40.21 m b.s.f.). The first and second bottom sub-unit were not resolved by the XRF data, but the microtomography indicates that their grains are similar in nature, both in size distribution and orientation. The third sub-unit within this event deposit at 40.21 m b.s.f. is different in nature, with smaller aspect ratio and finer grains. Grains of this sub-unit are notably different from the previous two sub-units in that there is a predominantly horizontal orientation to the grains.



This suggests that the third sub-unit is either related to a secondary deposition phase with a different content, was subjected to different energy/flow dynamics and/or followed a depositional mechanism different from the one responsible for the first two sub-units. The turbidite in U-Channel 6 (Fig. 7C) shows three sub-units with heavier grains (at *ca* 20.255, *ca* 20.237 and *ca* 20.23 m b.s.f.), which are only faintly indicated by the XRF-ratios, but more easily distinguished through microtomography. The lower turbidite sub-unit has a higher aspect ratio and higher concentration of heavy grains than the other two pulses, again indicating a variability between the different sub-units.

#### *Qualitative observations of event deposit structures*

X-ray microtomography contributes to our understanding of the origin of the material, the detailed layering, and the texture of sedimentary event deposits, particularly homogenites. Homogenites were previously analysed using core images and magnetic fabric (AMS). This study benefits from more direct views of the grain fabric using high-resolution 3D microtomography particularly for U-channel portions that contrast in density. Figure 8 shows zoom-ins of sedimentary structures from U-Channels 4 and 6 (additional X-ray microtomography images for U-Channels 2 and 8 are shown in Fig. S5). The images are shown without interpretation in Fig. S6. Focusing on the basal surface, internal basal structure of the turbidite unit and the base of the homogenite interval, several key observations are highlighted:

- The irregular shape of the base of the turbiditic interval for the thickest observed TuHm event deposits (Fig. 8B), and more subtly the microfractured base of event deposits 2 and 4 of U-Channel 4 (Fig. 8A). In contrast, the single thinner Tu event deposit in U-Channel 4 (Fig. 8A, event deposit 5) displays a smooth planar basal surface. For U-Channel 4 event deposit 2 (Fig. 8A), below the base of the homogenite, a deformed interval involving fine-grained and slightly coarser layers was observed.
- A complex distribution of coarser siliciclastic grains in the turbiditic interval base for the observed TuHm event deposits with multiple turbiditic laminations (Fig. 8). Based upon TuHm event deposits investigated here, this structure appears complex, including several microfractured intervals within the coarser-

grained portions of the sedimentary event deposits. These intervals have transitional bases and tops, which also correspond to downward and upward reduction and eventual disappearance of the microfractures. This suggests that microfracturing developed only within sub-units having a favourable rheology (grain-size distribution), even if the forces resulting in microfracturing probably also acted on the finer-grained sub-units.

- The successive occurrence of low-angle cross-bedding in the turbidite of U-Channel 6, particularly clear in middle part of the turbidite (Fig. 8B). The opposite dips in this cross-bedding were verified systematically using 2D views under multiple angles, excluding the possibility that the dips are ripple/dune structures that only appear opposite under certain viewing angles.

## DISCUSSION

Before attempting to interpret the presented observations and measurements in terms of depositional mechanism (for example, bed-load, suspended load, *in situ* reworking, *etc.*) and triggering process (for example, gravity reworking, ground shaking, tsunami wave, *etc.*), previously published nomenclature and interpretations of sedimentary event deposits are briefly reviewed and summarized. Figure 9 shows a schematic illustration of the main types of event deposits discussed here, without detailed internal subdivisions.

### **Turbidites and homogenites: brief reminders**

Relationships between sediment-carrying bottom density currents and specific types of sedimentary deposits (i.e. turbidites; Fig. 9A, similar to Fig. 3B) were established half a century ago, following *in situ* observations, measurements and laboratory analyses of outcropping deep-water formations. The first model to describe the internal subdivisions of individual turbidite beds was that of the 'Bouma sequence' (Bouma, 1962), relating turbidites to gravity-driven flows evolving from fluidized slumps. Later on, several other models were proposed as well (for a review, see Talling *et al.*, 2012). Other types of sedimentary deposits, whose internal structure differs from that of the initial 'Bouma sequence', have also been attributed to concentrated, particle-laden, gravity flows (e.g. in Lowe, 1982;

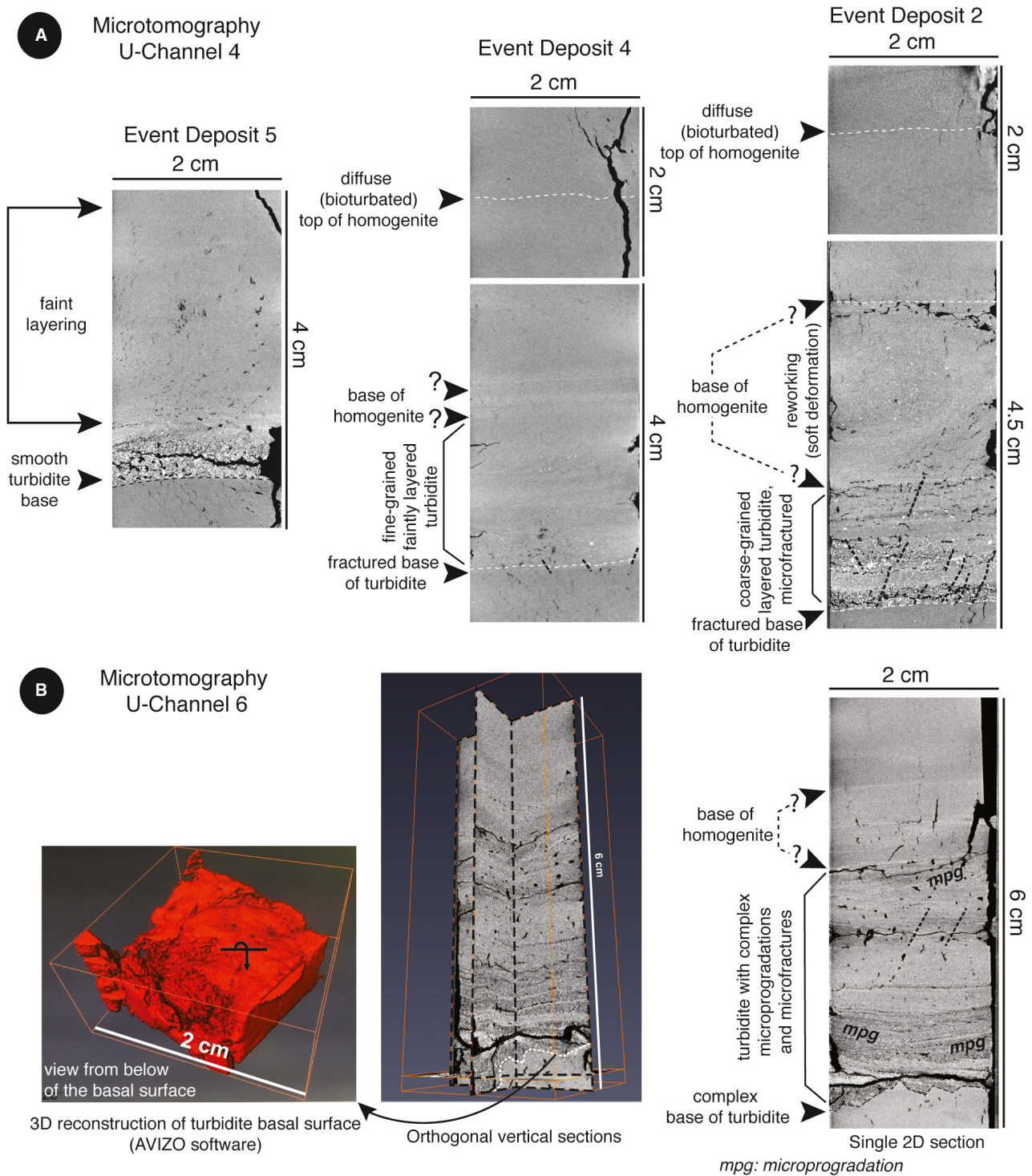


**Fig. 8.** X-ray microtomography examples for U-Channels 4 and 6. (A) Two-dimensional images of three sedimentary event deposits in U-Channel 4 (see position in Fig. 6). (B) Images of the sedimentary event deposit in U-Channel 6 (same interval as Fig. 7C), including the 3D view of the basal turbidite surface (left), orthogonal sections of the imaged interval (middle) and a single 2D section (right). Microprograding (*mpg*) features are displayed in 2D; additional microtomographic data on U-Channel 6 indicate that they display opposite senses.

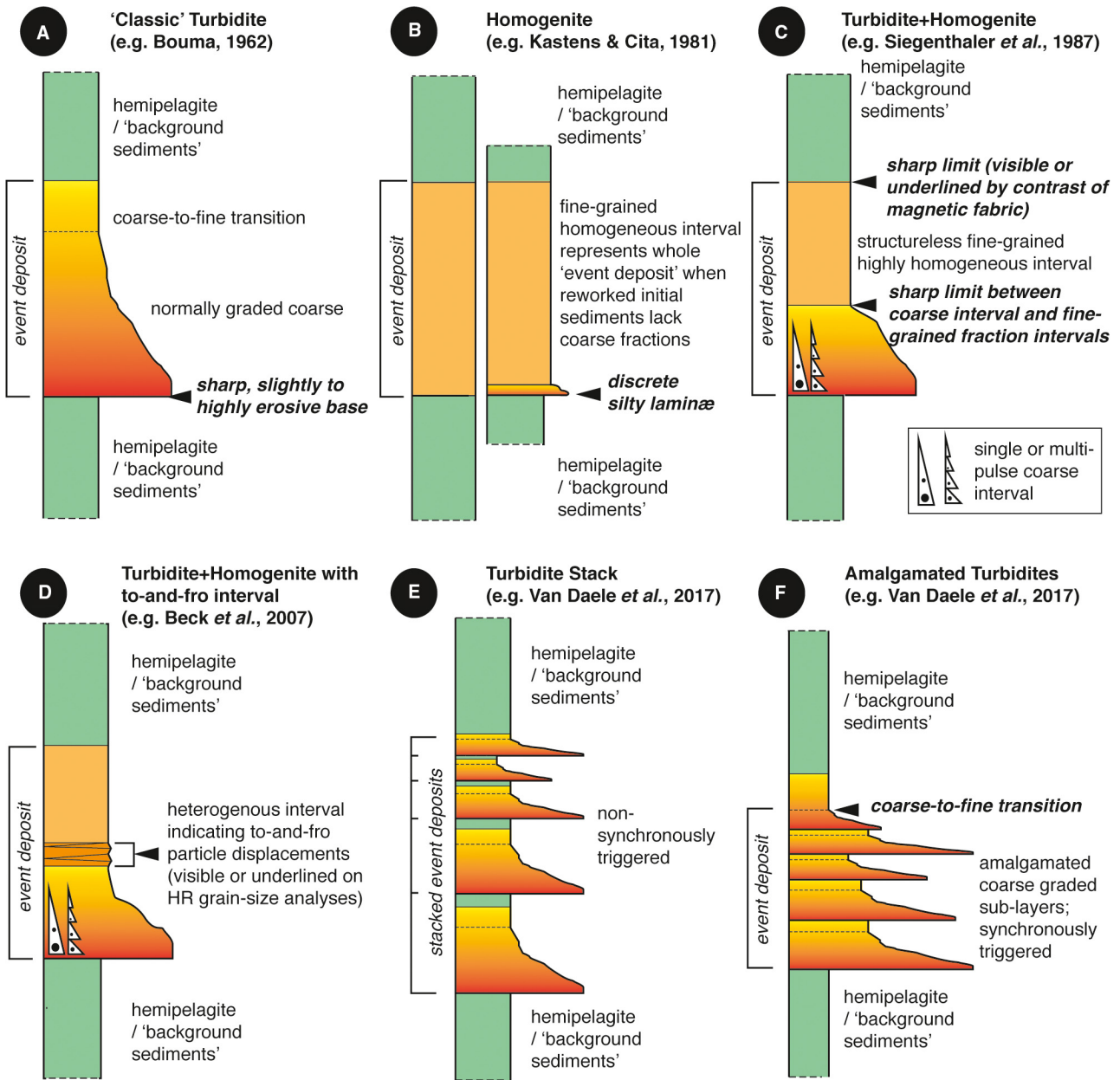


**Fig. 9.** Schematic examples of sedimentary event deposits. (A) 'Classic' turbidites; (B) homogenites; (C) turbidite+homogenite; (D) turbidite+homogenite with a 'to and fro' interval; (E) turbidite stack; and (F) amalgamated turbidites. See figure for references.

Stow & Wetzel, 1990; Stow, 1992). The significance of the initial internal subdivisions of a turbidite, *sensu* Bouma sequence, has been questioned by several authors, both with regard to the mechanical processes involved (e.g. Talling *et al.*, 2012) and to layers that are unrelated to gravity-driven flows (e.g. Shanmugam, 1997). Importantly, underflow prolongation of a river discharge (hyperpycnal flows) may produce

turbidites (Mulder & Syvitski, 1995), but should not be considered as a gravity-reworking event (e.g. Arnaud *et al.*, 2002; Beck, 2009).

High resolution surveys, both in marine and lacustrine settings (geophysical imaging and coring), have pointed out another type of reworking deposit consisting of anomalously thick, fine-grained, homogeneous sediment with little or no coarse fraction at the base (Fig. 9B). These

'unifites' (Stanley, 1981) or 'homogenites' (Kastens & Cita, 1981; Cita *et al.*, 1996; San Pedro *et al.*, 2017) were interpreted as resulting from tsunami wave impacts on the sea floor, and/or from seiches within a confined setting (Chapron *et al.*, 1999; Mulder *et al.*, 2009). In enclosed basins like the Gulf of Corinth, tsunamis are caused by displacement of the sea/lake floor during earthquakes and/or non-seismically triggered slumping, and a seiche is the harmonic resonance of waves within the basin as the tsunami is reflected and the water oscillates back and forth (e.g. Ichinose *et al.*, 2000). Both tsunamis and seiches affect the entire water column, and increase pore fluid pressure to facilitate erosion and deformation (see discussion in Alsop & Marco, 2012). The authors are not aware of any criteria to differentiate between seiche and tsunami-induced homogenites in enclosed basins like the Gulf of Corinth. As an alternative scenario to tsunami/seiche induced deposits, slope failure of fine-grained sediments with no or very little coarse fraction may also result in turbidity currents and homogenite deposition. A particular 3D structure is often reported for homogenite deposits: a large thickness, onlapping geometry in all directions, and no visible lateral transition to coarser layers or a mass-transport deposit (no visible 'root').

Additionally, different investigations in marine, as well as lacustrine, settings have described both: (i) turbidites displaying a sharp transition between the coarse, fining-upward, lower part and the homogeneous fine-grained upper sub-unit; and (ii) incomplete turbidites associated with a homogenite (Siegenthaler *et al.*, 1987; Sturm *et al.*, 1995; Beck *et al.*, 2007) (Fig. 9C, similar to Fig. 3A). Both cases are inferred to represent a unique instantaneous sedimentary event deposit for which the settling of the final fine-grained suspension requires an additional process apart from the final and/or distal damping of a single bottom monophasic turbidity current. Whereas the term 'Turbidite+Homogenite' (TuHm) is used here for

these deposits (as in Campos *et al.*, 2013a, 2013b; McHugh *et al.*, 2014), the authors note that others have referred to similar deposits as turbidites (e.g. Van Daele *et al.*, 2015), megaturbidites (Polonia *et al.*, 2013) or homogenites with a coarse base (Moernaut *et al.*, 2017). The link of turbidite+homogenite deposition with slope failure followed by tsunami waves and/or seiches is based on sediment textural analyses (Chapron *et al.*, 1999; Beck *et al.*, 2007; Campos *et al.*, 2013b) and on exceptional post-earthquake *in situ* surveys (Thunell *et al.*, 1999; McHugh *et al.*, 2011; Lorenzoni *et al.*, 2012; Van Daele *et al.*, 2015). Alternatively, if a large amount of re-mobilized fine-grained sediment ends up in suspension following slope failure, tsunamis and/or seiches may not necessarily be involved.

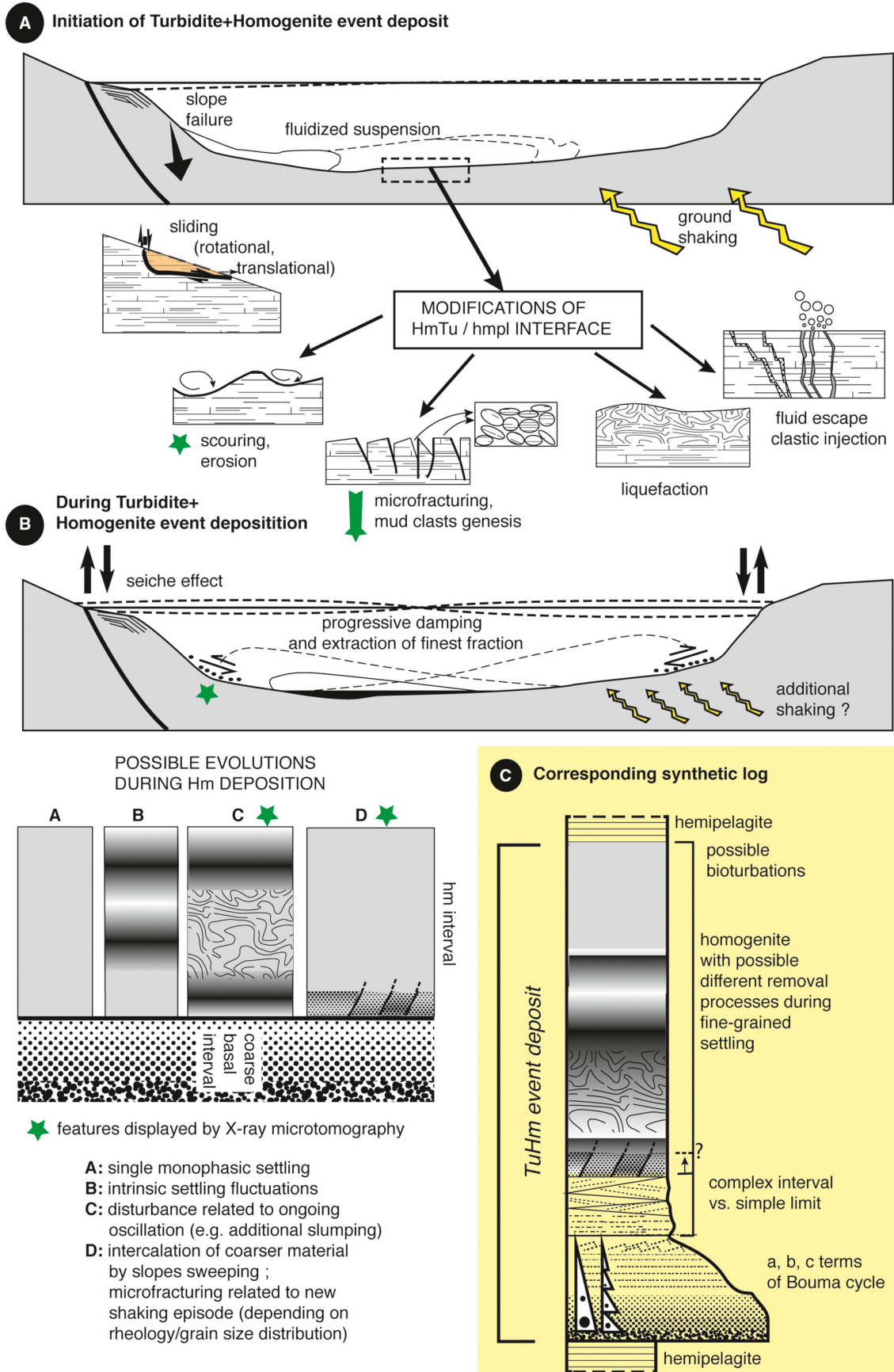
In some cases, evidence of 'to and fro' bottom currents have been observed between the two sub-units of TuHm deposits (Fig. 9D; Beck *et al.*, 2007; Campos *et al.*, 2013a), represented by thin silty laminae at the base of a single homogenite (Chapron *et al.*, 1999). Apart from single TuHm deposits, multiple TuHm may be separated by little or no hemipelagic interval (Van Daele *et al.*, 2017). For such cases, this study underlines the difference between a unique event deposit with multiple fining-upward sub-units resulting in an amalgamated turbidite (Fig. 9E) and a separate, stacked event deposit occurring with a high frequency (Fig. 9F).

Sharp grain-size breaks within sedimentary event deposits, as in TuHm deposits, have also been described in relation to a bimodal grain-size distribution within a flow (e.g. Kane *et al.*, 2007), reflective flows (Pickering & Hiscott, 1985), flow separation due to topographic obstacles (Sinclair & Cowie, 2003), vertical flow stratification (Gladstone & Sparks, 2002) and fluctuations in flow capacity (Kneller & McCaffrey, 2003), although none of these cases would result in the characteristic homogeneous fine-grained upper part of the deposit (see models in

---

**Fig. 10.** Explanatory model for TuHm event deposits from U-Channels 4 and 6: (A) initial triggering and different possible consequences: gravity reworking, water mass movement, and water/sediment interface disturbance; (B) possible additional effects on settling due to internal (a-A and a-B cases) or external factors (a-C and a-D cases); (C): conceptual model integrating the different inferred mechanisms. Green stars marks particularly well imaged features through X-ray microtomography. To simplify, only one gravity reworking site is represented, but several ones may occur simultaneously from different areas. Adapted from Chapron *et al.* (1999), Beck *et al.* (2007), Beck (2009), and completed.





Stevenson *et al.*, 2014). Alternatively, fluid mud layers can hinder the settling of non-cohesive grains that bypass these layers down-slope to form deposits with sand sharply separated from structureless mud, with the mud thickness increasing towards topographic lows (Stevenson *et al.*, 2014). The authors note that such a model could also result in deposits similar to turbidites+homogenites. Turbidite lofting resulting from suspension clouds in relation to hyperpycnal flows (Zavala *et al.*, 2011), or ‘dilute plume’ river deposition (Hiz-zett *et al.*, 2018; Hage *et al.*, 2019), could also result in sand–mud couplets with sharp transitions, but are typically more rhythmic in nature and more abundant in plant remains than surge-like gravity reworking deposits (Zavala & Acuri, 2016).

### Inferred depositional mechanisms Corinth Rift event deposits

#### *The classical view: from grain-size analysis, anisotropy of magnetic susceptibility and X-ray fluorescence studies*

Grain sizes are consistently fining-upward within all studied turbidites, and it is emphasized here that gradual or sharp changes clearly mark the difference between turbidite and TuHm sedimentary event deposits, respectively (Fig. 4). Similar to previous studies (e.g. Rothwell *et al.*, 2006; Konfirst *et al.*, 2011), this work found that Zr/Rb, Si/Al and Fe/Si appear to be useful chemical proxies for grain size, showing very similar trends to D50/D99 (Figs 6 and 7; Fig. S3). Our XRF results are generally in agreement with those of Campos (2014) for nearby sedimentary core MD01-2477 (Fig. 1), which show Ca/Fe, Ca/Ti and Ca/Si as good indicators of homogenites. As such, although a large part of the catchment in the Corinth Rift is carbonate-dominated (e.g. Gawthorpe *et al.*, 2018; Fig. 1), the overall lower Ca content of the reworked sediments suggests a higher siliciclastic detrital content for event beds compared to the more biogenic hemipelagites. Homogenites may represent either allochthonous material or *in situ* reworking (re-suspension and re-settling) of fine-grained material; the difference in composition between homogenites and hemipelagites favours the former.

The present AMS results are also similar to previous findings (Campos *et al.*, 2013b; Maffione & Morris, 2017) in the sense that homogenites are characterized by high foliation (Figs 6

and 7) and corrected anisotropy degree Pj (Fig. S4). For future work on sedimentary event deposits in the IODP-381 cores, the XRF results appear to be particularly useful given their ability to help distinguish >2 cm thick turbidites and homogenites from hemipelagites (Figs 5, 6 and 7) and their availability at 2 cm resolution for most of borehole M0079A (McNeill *et al.*, 2019a).

In addition to confirming previous findings using classical parameters, as mentioned above, our detailed microtomographic analysis highlights two novel observations. Firstly, lower Tu sub-units with bedding that is complex, multi-layered, coarse and overall normal graded, appear to be the rule rather than the exception. Given the scale of the analysis, Campos *et al.* (2013a) did not resolve this in their study of comparable deposits in the Corinth Rift. Secondly, several homogenite sections of TuHm event deposits actually consist of multiple intervals. This subdivision is different from previously published cases where a homogenite gradually changes upward from faintly layered to structureless (Beck *et al.*, 2019). Here, the transition (Hm1/Hm2 on Figs 6, 7C and 7D) involves sharp changes in chemical and textural parameters. These two findings are discussed briefly in the following section.

#### *A more complex view from X-ray microtomography images*

Although our results concern short portions of selected sedimentary event deposits, both the turbiditic base and the overlying homogenite of a TuHm deposit reveal a distinct complexity when imaged through X-ray microtomography (Figs 8 and 10).

Concerning the basal parts of TuHm deposits, from base to top, the following are highlighted: (1) The occurrence of complex basal surfaces. The curved shapes (Fig. 8B) are interpreted to be formed by erosion of a dense coarse flow; due to the small size of the U-channel, only part of a groove cast-type surface may have been crossed (Fig. 10A). The planar subvertical shapes (Fig. 8B) are interpreted as microfractures in the underlying mud, before the arrival of the basal turbidite (Fig. 10A). Following the criteria in McNeill *et al.* (2019a), the authors prefer this interpretation over drilling-induced fractures because they are planar and do not appear to be influenced by the core liner or core axis orientation. Generally, the upper sections of the boreholes investigated here are relatively

well-preserved with little coring disturbance, as they were drilled in push mode (McNeill *et al.*, 2019a). In the studied core sections, neither liquefaction nor fluid-escape features were observed (Fig. 10A), as mentioned elsewhere at the turbidite/hemipelagite interface (e.g. Beck *et al.*, 2007). The difference between an irregular and a smooth turbidite base (Fig. 8) may be explained by more friction at the base of the turbid flow (irregular base) *versus* a total decoupling (smooth base), or by variable erosion in relation to energy of the flow. (2) Within the coarser-grained lower part of U-Channel 6 (Fig. 8B), clear low-angle cross-bedding was observed (in 2D and 3D). Classical schematic subdivision of turbidites (e.g. Bouma, 1962) often indicates, in this position, climbing ripples following a unique flow direction. Here, successive opposite directions are interpreted as an effect of complex flow patterns similar to previously described ‘to and fro’ intervals (Campos *et al.*, 2013a) or reflected turbidites (Pickering & Hiscott, 1985). Alternatively, amalgamated turbidites originating from different slopes may also show different flow directions (e.g. Wils *et al.*, 2021), but clear coarsening between separate pulses was not observed here (Van Daele *et al.*, 2017) so this interpretation is not favoured. (3) Faint turbidite layering, related to progressive grain-size distribution changes, fitting the description of amalgamated turbidites (Van Daele *et al.*, 2017). In two cases (event deposit 2 in U-Channel 4, Fig. 8A and the event deposit in U-Channel 6, Fig. 8B), microfractures are concentrated within the coarser sub-units.

As mentioned in the *Correlations of geochemical, magnetic and textural parameters and X-ray micro-tomography data* sections, several homogenite sections of TuHm event deposits appear to consist of separate sub-units on split core surface and X-ray images [U-Channel 4 (40.04 and 40.175 m b.s.f., event deposits 2 and 4, Fig. 6); and U-Channel 6 (20.15 m b.s.f., Fig. 7; as well as U-Channels 2, 5, 7 and 8; Figs S3 and S4, and Table S1)]. The XRF profiles show changes between the homogenite sub-units, but not in a consistent manner in the three examples in U-Channels 4 and 6. X-ray microtomography adds two observations concerning the Hm-subdivision: subtle density differences between the homogenite sub-units in U-Channel 4 (Fig. 6) and faint laminations at the base of the lower homogenite sub-units in U-Channel 6 (Fig. 7). The homogenite subdivision is related to two settling phases: initial high-

density suspension behaviour followed by longer lasting settling from a stable suspension. The observed XRF and structural variations imply that non-uniform settling is guided by the composition of the initial suspension and by slight segregations among suspended particles (Fig. 10B, case B).

Details displayed by X-ray microtomography also question the location of the TuHm transition, especially for event deposit 2 of U-Channel 4 (Fig. 8A) and U-Channel 6 (Fig. 8B). In U-Channel 6, two similar fine-grained sub-units overlie cross-stratified coarser laminations. The lower one may represent a Hm1, overlain by a Hm2, as mentioned above, and interpreted as a change in settling (intrinsic cause; for example, evolution from a high-density suspension to lower-density one). The authors propose a similar interpretation for the faint layering within U-Channel 4 event deposit 4 (Fig. 10B, case B). The soft-sediment deformation within U-Channel 4 (event deposit 2; Fig. 8A), which was interpreted as slumping, occurred after the beginning of suspension settling; this disturbed sub-unit may be considered as part of the homogenite (Fig. 10B case C, and Fig. 10C). This feature, as well as microfractures within the turbiditic unit and possibly within a transition interval (Fig. 10C), clearly represents a post-turbidite disturbance. If the initial turbidite was earthquake-related, this post-turbidite disturbance may be related either to ongoing strong oscillations or to new shaking events, possibly aftershocks.

Several authors have described, at the TuHm transition, coarser lamina that they relate to remobilization of shallow-water sediments (Chapron *et al.*, 1999; Moernaut *et al.*, 2017); such surficial remobilization has been clearly demonstrated for major subduction earthquakes and tsunamis, using short-lived radiogenic isotopes (McHugh *et al.*, 2016). For large closed basins, a sharp thermocline may be affected by internal Kelvin waves that erode soft sediments where the thermocline impinges on the slope (Bouffard & Lemmin, 2013). This process may have played a role as well within the Gulf of Corinth (Fig. 10B, case D), and could explain the complexities observed within the homogenite deposits.

#### *Depositional mechanisms of IODP-381 sedimentary event deposits*

The most common triggers of sedimentary event deposits are earthquakes, tsunamis, seiches, coastal/subaqueous landslides and/or floods. For

the larger event deposits studied here, like event deposit 2 in U-Channel 4 (*ca* 10 cm) and the event deposit in U-Channel 6 (*ca* 20 cm), seismic or aseismic slope failures followed by a tsunami/seiche were found to be the most straightforward interpretation, given the complex turbidite base, microfracturing and evidence for ongoing oscillations (Fig. 10).

Assuming a uniform seismic attenuation relationship for the Corinth region, the earthquakes responsible for triggering mass wasting should be the ones strongest and closest to unstable slopes (Ambraseys, 1988). The faults and the slopes on the southern basin margin (Fig. 1) therefore seem the most likely source for such events: the faults are the Rift's largest in terms of throw (Fernández-Blanco *et al.*, 2019b) and have the highest late Quaternary slip rates (Nixon *et al.*, 2016). Given the asymmetry of the half-graben (De Gelder *et al.*, 2019) the slopes are also steeper on the southern than the northern margin. The southern margin slopes near the coring sites extend from *ca* 100 m to *ca* 800 m b.s.l., dipping *ca* 20° in the upper slopes and more than 30° in the lower slopes (Charalampakis *et al.*, 2014), and have been shown to be highly unstable (Ferentinos *et al.*, 1988; Lykousis *et al.*, 2009). High-resolution seismic profiles at the coring sites are lacking, but at the base of the lower slopes along most of the southern margin, several mass-transport deposits have been observed on seismic data (Ferentinos *et al.*, 1988; Charalampakis *et al.*, 2014), indicating that gravity reworking was likely the main cause of the event deposits. As mentioned before, gravity reworking/subaqueous landslides in the Corinth Rift can also be triggered aseismically, specifically during the rainy season when high sediment influx is causing slope instabilities near river mouths (Galanopoulos *et al.*, 1964; Heezen *et al.*, 1966). On the basin floor of the West Corinth Rift, six out of seven sedimentary event deposits were correlated with historical earthquakes, and only one to an aseismic submarine landslide (Beckers *et al.*, 2017). As such, the authors also suspect that most of the sedimentary event deposits in the IODP-381 cores showing evidence for gravity reworking are earthquake triggered. In terms of tsunamis, historical tsunamis in the Corinth Rift have ranged in run-up height from some tens of centimetres to several metres, with 15 out of 17 events (compilation in Kortekaas *et al.*, 2011) related to earthquakes and two to aseismic landslides. Even if coastal damage was minor for some of

these events, it is emphasized here that homogenite deposition on the basin floor would mostly result from fine-grained material ending up in suspension during subaqueous slope failures and surficial remobilization (McHugh *et al.*, 2016). Although it is not straightforward to distinguish these two sources, the preservation potential of basin-floor tsunami deposits seems greater than that of the often-incomplete near-shore and beach environments (Alsop & Marco, 2012). To better resolve the possible link between earthquakes/tsunamis and sedimentary event deposits in the Corinth Rift, future work will focus on a detailed comparison with the palaeoseismic and palaeotsunami record, supported by radiocarbon dating of event deposits, but this is beyond the scope here.

In contrast to the larger (>10 cm) event deposits mentioned above, for smaller event deposits without a complex turbidite base, microfracturing and evidence for ongoing oscillations, like event deposit 3 in U-Channel 4 (*ca* 2 cm), the authors consider processes other than gravity reworking similarly possible. As mentioned before (*Turbidites and homogenites: brief reminders* section), the sharp grain-size breaks within the TuHm deposits can also be interpreted as the result of turbidite lofting (Zavala *et al.*, 2011) or fluid mud layers that hinder the settling of non-cohesive grains (Stevenson *et al.*, 2014). In future work, one possible way to help distinguish the depositional mechanism is to look in more detail to organic content within the sedimentary event deposits (Zavala & Arcuri, 2016).

#### *Possible effect of the depositional environments on structure/composition of sedimentary event deposits*

All previous remarks on specific layers can also be discussed within the context of two depositional environments; marine and SI. In neighbouring core MD01-2477, although only covering *ca* 6 ka of the SI interval, Campos *et al.* (2013a) mention generally thicker sedimentary event deposits within the marine interval compared to the underlying SI interval. They tentatively attribute this tendency to more available detrital material in source areas; the authors consider that erosional products may have been stored at shallow depths during the Last Glacial Maximum, and mobilized later during the Holocene. With an average 13 cm for the nine marine sedimentary event deposits and 12 cm for the



ten SI event deposits, such a trend cannot be observed here, but the present number of samples is too small to draw robust conclusions. Other studies have also focused on differences in sedimentary event frequency during glacial and Holocene times (e.g. Beck *et al.*, 2007), in relation to changes in erosion/sedimentation rates, sea-level and shelf geometry. Such an analysis is beyond the scope of this study, but it is noted that the hypothesis of thicker and less frequent event deposits during marine periods can be easily tested in a future study on sedimentary event deposit size and frequency over a larger vertical section.

Concerning the combined thickness of sedimentary event deposits and hemipelagic deposition, McNeill *et al.* (2019b) showed on the longer IODP-381 cores that sedimentation rates and the input of coarse material (sands, silts) are generally lower during marine than in SI intervals. Similar to Collier *et al.* (2000), they conclude that both reduction and change of vegetation cover led to stronger soil erosion and higher sediment flux into the basin during the SI intervals. In the core portions investigated here, two major differences were found between marine and SI environments: (i) Higher Sr and Sr/Ti concentrations within the SI interval (Fig. 5 and Fig. S2), particularly for hemipelagic sedimentation. This was related to the aragonite needles occurring more frequently within the SI interval than in the marine interval, especially in the transition from marine to SI environments (Campos, 2014; McNeill *et al.*, 2019a,b). Their occurrence is a possible consequence of either *in situ* mixing of marine and freshwater, or precipitation in shallow areas and subsequent remobilization and transport (Moretti *et al.*, 2004; Lykousis *et al.*, 2007); (ii) Hemipelagites seem to be more sensitive to environmental changes than homogenites, specifically for Ti/Sr, Zr/Rb, Ti/Rb and Zr/K (Fig. 5). This suggests that similar fine-grained deposits are reworked during both marine and SI conditions, even if *in situ* hemipelagic deposition changes. The authors envision that differences in water depth and shelf geometry during marine and SI conditions could affect tsunami/seiche generation and thus homogenite thickness and structure, but in the present limited homogenite sample size this cannot be observed.

Both of the findings mentioned above concern hemipelagic deposition rather than sedimentary event deposits. As such, the authors consider that to a first order the depositional processes inferred for sedimentary event deposits on the Corinth Rift basin floor are similar in marine

and SI environments in terms of thickness, structure and composition.

## CONCLUSIONS AND PERSPECTIVES

The main goal of the present investigation is to improve current understanding of sedimentary event deposits in the Central Gulf of Corinth during the last *ca* 25 ka, using a combination of grain-size, magnetic and chemical parameters with high-resolution X-ray microtomography. We highlight the following outcomes of these analyses.

**1** Grain-size, anisotropy of magnetic susceptibility (AMS) and X-ray fluorescence (XRF) measurements provide efficient means to distinguish sedimentary event deposits (turbidite and turbidite+homogenite – ‘TuHm’ – deposits) from hemipelagic background sediments for the event deposits recorded within boreholes M0078B and M0079A of IODP Expedition 381. X-ray microtomography is complementary to those measurements because it provides observations of differences in density and texture down to the clay/silt grain-scale.

**2** X-ray microtomography evidences the complexity of basal turbidites within a sedimentary event deposit. Three-dimensional imaging can detect microfractures and erosional features relating to the basal surface, and multiple coarse-grained turbiditic sub-units (Fig. 10), which are interpreted here as expressions of complex gravity flows. Successive cross-bedded sets, dipping in opposite directions, are interpreted as indicative of water mass oscillations typical for tsunamis/seiches or due to turbidite reflection within the enclosed Gulf.

**3** X-ray microtomography helps in detecting faint layering (sometimes folded) within homogenites, possibly related to discrete changes in composition and grain size. These features are interpreted as indications of intrinsic settling fluctuations, ongoing water mass displacement during homogenite deposition and/or the intercalation of coarser material during subsequent gravity flows (Fig. 10B).

**4** The larger (>10 cm) event deposits studied here were interpreted as the result of seismic or aseismic slope failures followed by tsunami/seiche waves, given the complex turbidite base, microfracturing and evidence for ongoing oscillations. For smaller event deposits where this was not observed, other processes were also considered possible, like hyperpycnal flows and sediment lofting.

5 In terms of environmental influences on sedimentary event deposits, XRF results indicate that turbidites and homogenites are less sensitive to changes between marine and (semi-) isolated conditions than the hemipelagic sedimentation. Within the present limited sample size major differences in terms of sedimentary event deposit thickness, composition and structure were not observed.

In a general sense, X-ray microtomography can document characteristics of all types of sedimentary event deposits to better understand their origins. More specifically, it can provide additional observations that assist in the interpretation of the seismic/tsunami origins, and help achieve a chronicle of regional palaeoseismicity, either in the Corinth Rift or elsewhere.

## ACKNOWLEDGEMENTS

We sincerely thank Marc de Batist and one anonymous reviewer for thorough and constructive reviews that improved this manuscript. This research used samples and/or data provided by the International Ocean Discovery Program (IODP). Funding for this research was provided by IODP-France. GdG and CS thank IODP-France for the financial support and postdoctoral scholarship that helped us carry out this research. GC publishes with permission of the Director of the British Geological Survey (United Kingdom Research and Innovation). RLG thanks the VISTA programme of Norwegian Academy of Science and Letters for the award of its VISTA Professorship which also provided support to SP in order to undertake research on IODP Expedition 381, and RLG also acknowledges support from the Research Council of Norway (DeepRift project; number 308805). We thank OSUG@2020 for its contribution to the X-ray microtomography funding and Pierre Lhuissier from the SIMAP laboratory for his help in performing X-ray tomography acquisition. We thank all IODP-381 expedition members for insightful discussions on a wide spectrum of topics in relation to the Corinth Rift. All authors declare that there are no conflicts of interest in relation to this article.

## DATA AVAILABILITY STATEMENT

Preliminary results of the whole OSP and raw data of IODP Expedition 381 (Expedition Report) are accessible on <http://www.ecord.org/expedition>

381/. Additional data that support the findings of this study are available from the corresponding author upon reasonable request.

## REFERENCES

- Alsop, G.I.** and **Marco, S.** (2012) Tsunami and seiche-triggered deformation within offshore sediments. *Sed. Geol.*, **261–262**, 90–107.
- Ambraseys, N.N.** (1988) Engineering seismology, *Earthquake Eng. Struct. Dyn.*, **17**, 1–105.
- Armijo, R., Meyer, B., King, G.C.P., Rigo, A.** and **Papanastassiou, D.** (1996) Quaternary evolution of the Corinth Rift and its implications for the Late Cenozoic evolution of the Aegean. *Geophys. J. Int.*, **126**(1), 11–53.
- Arnaud, F., Lignier, V., Revel, M., Desmet, M., Beck, C., Pourchet, M., Charlet, F., Trentesaux, A.** and **Tribouillard, N.** (2002) Flood and earthquake disturbance of 210Pb geochronology (Lake Anterne, NW Alps). *Terra Nova*, **14**(4), 225–232.
- Beck, C.** (2009) Late Quaternary lacustrine paleo-seismic archives in north-western Alps: Examples of earthquake-origin assessment of sedimentary disturbances. *Earth Sci. Rev.*, **96**(4), 327–344.
- Beck, C., Campos, C., Eriş, K.K., Çağatay, N., Mercier de Lépinay, B. and Jouanne, F.** (2015) Estimation of successive coseismic vertical offsets using coeval sedimentary events—application to the southwestern limit of the Sea of Marmara's Central Basin (North Anatolian Fault). *Nat. Hazard. Earth Syst. Sci.*, **15**(2), 247–259.
- Beck, C., Carrillo, E., Audemard, F., van Welden, A.** and **Disnar, J.-R.** (2019) Tentative integration of paleoseismic data from lake sediments and from nearby trenches: the central section of the Boconó Fault (northern Venezuela). *J. S. Am. Earth Sci.*, **92**, 646–657.
- Beck, C., Mercier de Lépinay, B., Schneider, J.-L., Cremer, M., Çağatay, N., Wendenbaum, E., Boutareaud, S., Ménot, G., Schmidt, S., Weber, O., Eris, K., Armijo, R., Meyer, B., Pondard, N., Gutscher, M.-A., Turon, J.-L., Labeyrie, L., Cortijo, E., Gallet, Y., Bouquerel, H., Gorur, N., Gervais, A., Castera, M.-H., Londeix, L., de Rességuier, A. and Jaouen, A.** (2007) Late Quaternary co-seismic sedimentation in the Sea of Marmara's deep basins. *Sed. Geol.*, **199**(1), 65–89.
- Beck, C., Reyss, J.-L., Leclerc, F., Moreno, E., Feuillet, N., Barrier, L., Beauducel, F., Boudon, G., Clément, V., Deplus, C., Gallou, N., Lebrun, J.-F., Le Friant, A., Necessian, A., Paterné, M., Pichot, T. and Vidal, C.** (2012) Identification of deep subaqueous co-seismic scarps through specific coeval sedimentation in Lesser Antilles: implication for seismic hazard. *Nat. Hazard. Earth Syst. Sci.*, **12**(5), 1755–1767.
- Beckers, A., Beck, C., Hubert-Ferrari, A., Reyss, J.-L., Mortier, C., Albini, P., Rovida, A., Develle, A.-L., Tripsanas, E., Sakellariou, D., Crouzet, C. and Scotti, O.** (2017) Sedimentary impacts of recent moderate earthquakes from the shelves to the basin floor in the western Gulf of Corinth. *Mar. Geol.*, **384**, 81–102.
- Beckers, A., Hubert-Ferrari, A., Beck, C., Papatheodorou, G., de Batist, M., Sakellariou, D., Tripsanas, E. and Demoulin, A.** (2018) Characteristics and frequency of large submarine landslides at the western tip of the Gulf of Corinth. *Nat. Hazard. Earth Syst. Sci.*, **18**(5), 1411–1425.

- Bell, R.E., McNeill, L.C., Bull, J.M., Henstock, T.J., Collier, R.E.L. and Leeder, M.R. (2009) Fault architecture, basin structure and evolution of the Gulf of Corinth Rift, central Greece. *Basin Res.*, **21**(6), 824–855.
- Bell, R.E., McNeill, L.C., Henstock, T.J. and Bull, J.M. (2011) Comparing extension on multiple time and depth scales in the Corinth Rift, Central Greece. *Geophys. J. Int.*, **186**(2), 463–470.
- Bernard, P., Lyon-Caen, H., Briole, P., Deschamps, A., Boudin, F., Makropoulos, K., Papadimitriou, P., Lemeille, F., Patau, G., Billiris, H., Paradissis, D., Papazissi, K., Castarède, H., Charade, O., Nercessian, A., Avallone, A., Pacchiani, F., Zahradnik, J., Sacks, S. and Linde, A. (2006) Seismicity, deformation and seismic hazard in the western rift of Corinth: New insights from the Corinth Rift Laboratory (CRL). *Tectonophysics*, **426**(1), 7–30.
- Bouffard, D. and Lemmin, U. (2013) Kelvin waves in Lake Geneva. *J. Great Lakes Res.*, **39**(4), 637–645.
- Bouma, A.H. (1962). *Sedimentology of some Flysch Deposits: A Graphic Approach to Facies Interpretation*. Elsevier, Amsterdam, 168 pp.
- Briole, P., Rigo, A., Lyon-Caen, H., Ruegg, J.C., Papazissi, K., Mitsakaki, C., Balodimou, A., Veis, G., Hatzfeld, D. and Deschamps, A. (2000) Active deformation of the Corinth rift, Greece: Results from repeated Global Positioning System surveys between 1990 and 1995. *J. Geophys. Res.*, **105**(B11), 25605–25625.
- Campos, C. (2014) *Comparative Study of Co-Seismic Sedimentation in Two Tectonically Active Areas: the Sea of Marmara and the Gulf of Corinth. Methodological Developments, Implication for Seismic Hazards Assessment*. PhD Thesis Memoir. Université Grenoble-Alpes, Grenoble, France, 248 pp.
- Campos, C., Beck, C., Crouzet, C., Carrillo, E., Van Welden, A. and Tripsanas, E. (2013a) Late Quaternary paleoseismic sedimentary archive from deep central Gulf of Corinth: time distribution of inferred earthquake-induced layers. *Annal. Geophys.*, **56**(6), 1–15. <https://doi.org/10.4401/ag-6226>.
- Campos, C., Beck, C., Crouzet, C., Demory, F., Van Welden, A. and Eris, K. (2013b) Deciphering hemipelagites from homogenites through anisotropy of magnetic susceptibility. Paleoseismic implications (Sea of Marmara and Gulf of Corinth). *Sed. Geol.*, **292**, 1–14.
- Chapron, E., Beck, C., Pourchet, M. and Deconinck, J.-F. (1999) 1822 earthquake-triggered homogenite in Lake Le Bourget (NW Alps). *Terra Nova*, **11**(2–3), 86–92.
- Charalampakis, M., Lykousis, V., Sakellariou, D., Papatheodorou, G. and Ferentinos, G. (2014) The tectono-sedimentary evolution of the Lechaion Gulf, the south eastern branch of the Corinth graben, Greece. *Mar. Geol.*, **351**, 58–75.
- Cita, M.B., Camerlenghi, A. and Rimoldi, B. (1996) Deep-sea tsunami deposits in the eastern Mediterranean: New evidence and depositional models. *Sed. Geol.*, **104**(1), 155–173.
- Collier, R.E.L., Leeder, M.R., Trout, M., Ferentinos, G., Lyberis, E. and Papatheodorou, G. (2000) High sediment yields and cool, wet winters: Test of last glacial paleoclimates in the northern Mediterranean. *Geology*, **28**(11), 999–1002.
- Cornet, F.H., Doan, M.L., Moretti, I. and Borm, G. (2004) Drilling through the active Aigion Fault: the AIG10 well observatory. *C.R. Geosci.*, **336**(4), 395–406.
- Croudace, I.W., Rindby, A. and Guy Rothwell, R. (2006) ITRAX: description and evaluation of a new multi-function X-ray core scanner. *Geol. Soc. London Spec. Public.*, **267**(1), 51–63.
- Ferentinos, G., Papatheodorou, G. and Collins, M.B. (1988) Sediment Transport processes on an active submarine fault escarpment: Gulf of Corinth, Greece. *Mar. Geol.*, **83**(1), 43–61.
- Fernández-Blanco, D., de Gelder, G., Lacassin, R. and Armijo, R. (2019a) *Geometry of Flexural Uplift by Continental Rifting in Corinth*. Tectonics, Greece. <https://doi.org/10.1029/2019TC005685>
- Fernández-Blanco, D., de Gelder, G., Lacassin, R. and Armijo, R. (2019b) A new crustal fault formed the modern Corinth Rift. *Earth-Sci. Rev.*, **199**, 102919.
- Galanopoulos, A., Delimbasis, N.D. and Comninakis, P.E. (1964) A tsunami generated by a slide without a seismic shock. *Geol. Chron. Greece*, **16**, 93–110.
- Gawthorpe, R.L., Leeder, M.R., Kranis, H., Skourtsos, E., Andrews, J.E., Henstra, G.A., Mack, G.H., Muravchik, M., Turner, J.A. and Stamatakis, M. (2018) Tectono-sedimentary evolution of the Plio-Pleistocene Corinth rift, Greece. *Basin Res.*, **30**(3), 448–479.
- de Gelder, G., Fernández-Blanco, D., Melnick, D., Duclaux, G., Bell, R.E., Jara-Muñoz, J., Armijo, R. and Lacassin, R. (2019) Lithospheric flexure and rheology determined by climate cycle markers in the Corinth Rift. *Sci. Rep.*, **9**(1), 4260.
- de Gelder, G., Jara-Muñoz, J., Melnick, D., Fernández-Blanco, D., Rouby, H., Pedoja, K., Husson, L., Armijo, R. and Lacassin, R. (2020) How do sea-level curves influence modeled marine terrace sequences? *Quatern. Sci. Rev.*, **229**, 106132.
- Gladstone, C. and Sparks, R.S.J. (2002) The significance of grain-size breaks in turbidites and pyroclastic density current deposits. *J. Sediment. Res.*, **72**(1), 182–191.
- Goldfinger, C., Morey, A.E., Nelson, C.H., Gutiérrez-Pastor, J., Johnson, J.E., Karabanov, E., Chaytor, J. and Eriksson, A. (2007) Rupture lengths and temporal history of significant earthquakes on the offshore and north coast segments of the Northern San Andreas Fault based on turbidite stratigraphy. *Earth Planet. Sci. Lett.*, **254**(1), 9–27.
- Gràcia, E., Vizcaino, A., Escutia, C., Asioli, A., Rodés, Á., Pallás, R., Garcia-Orellana, J., Lebreiro, S. and Goldfinger, C. (2010) Holocene earthquake record offshore Portugal (SW Iberia): testing turbidite paleoseismology in a slow-convergence margin. *Quatern. Sci. Rev.*, **29**(9), 1156–1172.
- Hage, S., Cartigny, M.J.B., Sumner, E.J., Clare, M.A., Hughes Clarke, J.E., Talling, P.J., Lintern, D.G., Simmons, S.M., Silva Jacinto, R., Vellinga, A.J., Allin, J.R., Azpiroz-Zabala, M., Gales, J.A., Hizzett, J.L., Hunt, J.E., Mozzato, A., Parsons, D.R., Pope, E.L., Stacey, C.D., Symons, W.O., Vardy, M.E. and Watts, C. (2019) Direct Monitoring Reveals Initiation of Turbidity Currents From Extremely Dilute River Plumes. *Geophys. Res. Lett.*, **46**(20), 11310–11320.
- Heezen, B.C., Ewing, M. and Johnson, G.L. (1966) The Gulf of Corinth floor. *Deep Sea Res. Oceanogr. Abs.*, **13**(3), 381–411.
- Hizzett, J.L., Hughes Clarke, J.E., Sumner, E.J., Cartigny, M.J.B., Talling, P.J. and Clare, M.A. (2018) Which triggers produce the most erosive, frequent, and longest runout turbidity currents on deltas? *Geophys. Res. Lett.*, **45**(2), 855–863.
- Ichinose, G.A., Anderson, J.G., Satake, K., Schweickert, R.A. and Lahren, M.M. (2000) The potential hazard from

- tsunami and Seiche waves generated by large earthquakes within Lake Tahoe, California-Nevada. *Geophys. Res. Lett.*, **27**(8), 1203–1206.
- Jelinek, V.** (1981) Characterization of the magnetic fabric of rocks. *Tectonophysics*, **79**(3), T63–T67.
- Jolivet, L., Labrousse, L., Agard, P., Lacombe, O., Bailly, V., Lecomte, E., Mouthereau, F. and Mehl, C.** (2010) Rifting and shallow-dipping detachments, clues from the Corinth Rift and the Aegean. *Tectonophysics*, **483**(3), 287–304.
- Kane, I.A., Kneller, B.C., Dykstra, M., Kassem, A. and McCaffrey, W.D.** (2007) Anatomy of a submarine channel-levee: An example from Upper Cretaceous slope sediments, Rosario Formation, Baja California, Mexico. *Mar. Petrol. Geol.*, **24**(6), 540–563.
- Kastens, K.A. and Cita, M.B.** (1981) Tsunami-induced sediment transport in the abyssal Mediterranean Sea. *GSA Bulletin*, **92**(11), 845–857.
- Kneller, B.C. and McCaffrey, W.D.** (2003) The interpretation of vertical sequences in Turbidite Beds: The influence of longitudinal flow structure. *J. Sediment. Res.*, **73**(5), 706–713.
- Konfirst, M.A., Kuhn, G., Monien, D. and Scherer, R.P.** (2011) Correlation of Early Pliocene diatomite to low amplitude Milankovitch cycles in the ANDRILL AND-1B drill core. *Mar. Micropaleontol.*, **80**(3), 114–124.
- Kontopoulos, N. and Avramidis, P.** (2003) A late Holocene record of environmental changes from the Aliko lagoon, Egean, North Peloponnese, Greece. *Quatern. Int. J. Int. Union Quatern. Res.*, **111**(1), 75–90.
- Kortekaas, S., Papadopoulos, G.A., Ganas, A., Cundy, A.B. and Diakantoni, A.** (2011) Geological identification of historical tsunamis in the Gulf of Corinth, Central Greece. *Nat. Hazard. Earth Syst. Sci.*, **11**(7), 2029–2041.
- Koukouvelas, I.K., Katsanopoulou, D., Soter, S. and Xypolias, P.** (2005) Slip rates on the Helike Fault, Gulf of Corinth, Greece: new evidence from geoarchaeology. *Terra Nova*, **17**(2), 158–164.
- Leeder, M.R., Portman, C., Andrews, J.E., Collier, R.E.L., Finch, E., Gawthorpe, R.L., McNeill, L.C., Pérez-Arlucea, M. and Rowe, P.** (2005) Normal faulting and crustal deformation, Alkyonides Gulf and Perachora peninsula, eastern Gulf of Corinth rift, Greece. *J. Geol. Soc.*, **162**(3), 549–561.
- Lemeille, F., Chatoupis, F., Foumelis, M., Rettenmaier, D., Unkel, I., Micarelli, L., Moretti, I., Bourdillon, C., Guernet, C. and Müller, C.** (2004) Recent syn-rift deposits in the hangingwall of the Aigion Fault (Gulf of Corinth, Greece). *C.R. Geosci.*, **336**(4), 425–434.
- Lorenzoni, L., Benitez-Nelson, C.R., Thunell, R.C., Hollander, D., Varela, R., Astor, Y., Audemard, F.A. and Muller-Karger, F.E.** (2012) Potential role of event-driven sediment transport on sediment accumulation in the Cariaco Basin, Venezuela. *Mar. Geol.*, **307–310**, 105–110.
- Lowe, D.R.** (1982) Sediment gravity flows; II, Depositional models with special reference to the deposits of high-density turbidity currents. *J. Sediment. Res.*, **52**(1), 279–297.
- Lykousis, V., Roussakis, G. and Sakellariou, D.** (2009) Slope failures and stability analysis of shallow water prodeltas in the active margins of Western Greece, northeastern Mediterranean Sea. *Geologische Rundschau: Zeitschrift Fur Allgemeine Geologie*, **98**(4), 807–822.
- Lykousis, V., Sakellariou, D., Moretti, I. and Kaberi, H.** (2007) Late Quaternary basin evolution of the Gulf of Corinth: Sequence stratigraphy, sedimentation, fault-slip and subsidence rates. *Tectonophysics*, **440**(1), 29–51.
- Maffione, M. and Morris, A.** (2017) The onset of fabric development in deep marine sediments. *Earth Planet. Sci. Lett.*, **474**, 32–39.
- Marco, S. and Agnon, A.** (1995) Prehistoric earthquake deformations near Masada, Dead Sea Graben. *Geology*, **23**(8), 695–698.
- McCalpin, J.** (2009) Paleoseismology. In: *International Geophysics Series* (Ed. McCalpin, J.), Volume **95**, 2nd edn, pp. 1–613. Elsevier, Amsterdam, The Netherlands.
- McHugh, C.M.G., Braudy, N., Çağatay, M.N., Sorlien, C., Cormier, M.-H., Seeber, L. and Henry, P.** (2014) Seafloor fault ruptures along the North Anatolia Fault in the Marmara Sea, Turkey: Link with the adjacent basin turbidite record. *Mar. Geol.*, **353**, 65–83.
- McHugh, C.M., Kanamatsu, T., Seeber, L., Bopp, R., Cormier, M.-H. and Usami, K.** (2016) Remobilization of surficial slope sediment triggered by the A.D. 2011 Mw 9 Tohoku-Oki earthquake and tsunami along the Japan Trench. *Geology*, **44**(5), 391–394.
- McHugh, C.M.G., Seeber, L., Cormier, M.-H., Dutton, J., Çağatay, N., Polonia, A., Ryan, W.B.F. and Gorur, N.** (2006) Submarine earthquake geology along the North Anatolia Fault in the Marmara Sea, Turkey: A model for transform basin sedimentation. *Earth Planet. Sci. Lett.*, **248**(3), 661–684.
- McHugh, C.M., Seeber, L., Braudy, N., Cormier, M.-H., Davis, M.B., Diebold, J.B., Dieudonne, N., Douilly, R., Gulick, S.P.S., Hornbach, M.J., Johnson, H.E., Mishkin, K.R., Sorlien, C.C., Steckler, M.S., Symithe, S.J. and Templeton, J.** (2011) Offshore sedimentary effects of the 12 January 2010 Haiti earthquake. *Geology*, **39**(8), 723–726.
- McNeill, L.C., Cotterill, C.J., Bull, J.M., Henstock, T.J., Bell, R. and Stefatos, A.** (2007) Geometry and slip rate of the Aigion fault, a young normal fault system in the western Gulf of Corinth. *Geology*, **35**(4), 355–<https://doi.org/10.1130/G23281A.1>
- McNeill, L.C., Shillington, D.J. and Carter, G.D.O.** (2019a) Corinth Active Rift Development. *Proceedings of the International Ocean Discovery Program*, 381. <https://par.nsf.gov/biblio/10224878>
- McNeill, L.C., Shillington, D.J., Carter, G.D.O., Everest, J.D., Gawthorpe, R.L., Miller, C., Phillips, M.P., Collier, R.E.L., Cvetkoska, A., De Gelder, G., Diz, P., Doan, M.-L., Ford, M., Geraga, M., Gillespie, J., Hemelsdaël, R., Herrero-Bervera, E., Ismaiel, M., Janikian, L., Kouli, K., Le Ber, E., Li, S., Maffione, M., Mahoney, C., Machlus, M.L., Michas, G., Nixon, C.W., Oflaz, S.A., Omale, A.P., Panagiotopoulos, K., Pechlivanidou, S., Sauer, S., Seguin, J., Sergiou, S., Zakharova, N.V. and Green, S.** (2019b) High-resolution record reveals climate-driven environmental and sedimentary changes in an active rift. *Sci. Rep.*, **9**(1), 6519.
- Migeon, S., Weber, O., Faugeres, J.-C. and Saint-Paul, J.** (1998) SCOPIX: A new X-ray imaging system for core analysis. *Geo-Mar. Lett.*, **18**(3), 251–255.
- Moernaut, J., Van Daele, M., Strasser, M., Clare, M.A., Heirman, K., Viel, M., Cardenas, J., Kilian, R., Ladrón de Guevara, B., Pino, M., Urrutia, R. and De Batist, M.** (2017) Lacustrine turbidites produced by surficial slope sediment remobilization: A mechanism for continuous and sensitive turbidite paleoseismic records. *Mar. Geol.*, **384**, 159–176.
- Moretti, I., Lykousis, V., Sakellariou, D., Reynaud, J.-Y., Benziane, B. and Prinzhofer, A.** (2004) Sedimentation and subsidence rate in the Gulf of Corinth: what we learn



- from the Marion Dufresne's long-piston coring. *C.R. Geosci.*, **336**(4), 291–299.
- Mulder, T. and Syvitski, J.P.M.** (1995) Turbidity Currents Generated at River Mouths during Exceptional Discharges to the World Oceans. *J. Geol.*, **103**(3), 285–299.
- Mulder, T., Zaragosi, S., Razin, P., Grelaud, C., Lanfume, V. and Bavoil, F.** (2009) A new conceptual model for the deposition process of homogenite: Application to a cretaceous megaturbidite of the western Pyrenees (Basque region, SW France). *Sed. Geol.*, **222**(3), 263–273.
- Pallikarakis, A., Papanikolaou, I., Reicherter, K., Triantaphyllou, M., Dimiza, M. and Koukousioura, O.** (2019) Constraining the regional uplift rate of the Corinth Isthmus area (Greece), through biostratigraphic and tectonic data. *Zeitschrift Für Geomorphologie Supplementary Issues*, **62**(2), 127–142.
- Nixon, C.W., McNeill, L.C., Bull, J.M., Bell, R.E., Gawthorpe, R.L., Henstock, T.J., Christodoulou, D., Ford, M., Taylor, B., Sakellariou, D., Ferentinos, G., Papatheodorou, G., Leeder, M.R., Collier, R.E.LI., Goodliffe, A.M., Sachpazi, M. and Kranis, H.** (2016) Rapid spatiotemporal variations in rift structure during development of the Corinth Rift, central Greece. *Tectonics*, **35**(5), 1225–1248. <http://dx.doi.org/10.1002/2015tc004026>
- Pantosti, D., De Martini, P.M., Koukouvelas, I., Stamatopoulos, L., Palyvos, N., Pucci, S., Lemeille, F. and Pavlides, S.** (2004) Palaeoseismological investigations of the Aigion Fault (Gulf of Corinth, Greece). *C.R. Geosci.*, **336**(4), 335–342.
- Papadopoulos, G.A.** (2000) *Historical Earthquakes and Tsunamis in the Corinth Rift, Central Greece*. Institute of Geodynamics, Athens, Greece.
- Papadopoulos, G.A.** (2003) Tsunami hazard in the Eastern Mediterranean: strong earthquakes and tsunamis in the Corinth Gulf, Central Greece. *Nat. Hazards*, **29**(3), 437–464.
- Papatheodorou, G. and Ferentinos, G.** (1997) Submarine and coastal sediment failure triggered by the 1995, Ms = 6.1 R Aegion earthquake, Gulf of Corinth, Greece. *Mar. Geol.*, **137**(3–4), 287–304.
- Papazachos, B.C., Comninakis, P.E., Karakaisis, G.F., Karakostas, B.G., Papaioannou, C.A., Papazachos, C.B. and Scordilis, E.M.** (2000) A catalogue of earthquakes in Greece and surrounding area for the period 550BC–1999. *Publ. Geoph. Lab., Univ. of Thessaloniki*, **1**, 333.
- Passega, R.** (1964) Grain size representation by CM patterns as a geologic tool. *J. Sediment. Res.*, **34**(4), 830–847.
- Pechlivanidou, S., Cowie, P.A., Duclaux, G., Nixon, C.W., Gawthorpe, R.L. and Salles, T.** (2019) Tipping the balance: Shifts in sediment production in an active rift setting. *Geology*, **47**(3), 259–262.
- Pérouse, E., Chamot-Rooke, N., Rabaute, A., Briole, P., Jouanne, F., Georgiev, I. and Dimitrov, D.** (2012) Bridging onshore and offshore present-day kinematics of central and eastern Mediterranean: Implications for crustal dynamics and mantle flow. *Geochem. Geophys. Geosyst.*, **13**(9), 1–25. <https://doi.org/10.1029/2012gc004289>
- Pickering, K.T. and Hiscott, R.N.** (1985) Contained (reflected) turbidity currents from the Middle Ordovician Cloridorme Formation, Quebec, Canada: an alternative to the antidune hypothesis. *Sedimentology*, **32**(3), 373–394.
- Polonia, A., Bonatti, E., Camerlenghi, A., Lucchi, R.G., Panieri, G. and Gasperini, L.** (2013) Mediterranean megaturbidite triggered by the AD 365 Crete earthquake and tsunami. *Sci. Rep.*, **3**, 1285.
- Polonia, A., Nelson, C.H., Romano, S., Vaiani, S.C., Colizza, E., Gasparotto, G. and Gasperini, L.** (2017) A depositional model for seismo-turbidites in confined basins based on Ionian Sea deposits. *Mar. Geol.*, **384**, 177–198.
- Ratzov, G., Cattaneo, A., Babonneau, N., Déverchère, J., Yelles, K., Bracene, R. and Courboulex, F.** (2015) Holocene turbidites record earthquake supercycles at a slow-rate plate boundary. *Geology*, **43**, 331–334. <https://doi.org/10.1130/G36170.1>
- Rigo, A., Lyon-Caen, H., Armijo, R., Deschamps, A., Hatzfeld, D., Makropoulos, K., Papadimitriou, P. and Kassaras, I.** (1996) A microseismic study in the western part of the Gulf of Corinth (Greece): implications for large-scale normal faulting mechanisms. *Geophys. J. Int.*, **126**(3), 663–688.
- Rodríguez-Pascua, M.A., Calvo, J.P., De Vicente, G. and Gómez-Gras, D.** (2000) Soft-sediment deformation structures interpreted as seismites in lacustrine sediments of the Prebetic Zone, SE Spain, and their potential use as indicators of earthquake magnitudes during the Late Miocene. *Sed. Geol.*, **135**(1–4), 117–135.
- Rothwell, R.G. and Croudace, I.W.** (2015) Twenty Years of XRF Core Scanning Marine Sediments: What Do Geochemical Proxies Tell Us? In: *Micro-XRF Studies of Sediment Cores: Applications of a Non-Destructive Tool for the Environmental Sciences* (Eds Croudace, I.W. and Rothwell, R.G.), pp. 25–102. Springer, Dordrecht.
- Rothwell, R.G., Hoogakker, B., Thomson, J., Croudace, I.W. and Frenz, M.** (2006) Turbidite emplacement on the southern Balearic Abyssal Plain (western Mediterranean Sea) during Marine Isotope Stages 1–3: an application of ITRAX XRF scanning of sediment cores to lithostratigraphic analysis. *Geol. Soc. London Spec. Public.*, **267**(1), 79–98.
- San Pedro, L., Babonneau, N., Gutscher, M.-A. and Cattaneo, A.** (2017) Origin and chronology of the Augias deposit in the Ionian Sea (Central Mediterranean Sea), based on new regional sedimentological data. *Mar. Geol.*, **384**, 199–213.
- Siegenthaler, C., Finger, W., Kelts, K. and Wang, S.** (1987) Earthquake and seiche deposits in Lake Lucerne, Switzerland. *Eclogae Geol. Helv.*, **80**(1), 241–260.
- Sinclair, H.D. and Cowie, P.A.** (2003) Basin-floor topography and the scaling of turbidites. *J. Geol.*, **111**(3), 277–299.
- Shanmugam, G.** (1997) The Bouma Sequence and the turbidite mind set. *Earth-Sci. Rev.*, **42**(4), 201–229. [http://dx.doi.org/10.1016/s0012-8252\(97\)81858-2](http://dx.doi.org/10.1016/s0012-8252(97)81858-2)
- Stanley, D.J.** (1981) Unifites: structureless muds of gravity-flow origin in Mediterranean basins. *Geo-Mar. Lett.*, **1**(2), 77–83.
- Stefatos, A., Charalambakis, M., Papatheodorou, G. and Ferentinos, G.** (2006) Tsunamigenic sources in an active European half-graben (Gulf of Corinth, Central Greece). *Mar. Geol.*, **232**(1), 35–47.
- Stevenson, C.J., Talling, P.J., Masson, D.G., Sumner, E.J., Frenz, M. and Wynn, R.B.** (2014) The spatial and temporal distribution of grain-size breaks in turbidites. *Sedimentology*, **61**(4), 1120–1156.
- Stow, D.A.V.** (Ed.) (1992). *Deep-water turbidite systems. International Associations of Sedimentologists*, Reprint Series 3, Blackwell Sc. Publ., 473 pp.
- Stow, D.A.V. and Wetzell, A.** (1990). Hemiturbidite: a new type of deep-water sediment. *Proc. Ocean Drilling Prog. Sci. Res.*, **116**, 25–34.

- Sturm, M., Siegenthaler, C. and Pickrill, R.A.** (1995). Turbidites and “homogenites”—a conceptual model of flood and slide deposits. *Publication of IAS-16th Regional Meeting Sedimentology, Paris*, **22**, 140.
- Talling, P.J., Masson, D.G., Sumner, E.J. and Malgesini, G.** (2012) Subaqueous sediment density flows: Depositional processes and deposit types. *Sedimentology*, **59**(7), 1937–2003.
- Taylor, B., Weiss, J.R., Goodliffe, A.M., Sachpazi, M., Laigle, M. and Hirn, A.** (2011) The structures, stratigraphy and evolution of the Gulf of Corinth rift, Greece. *Geophys. J. Int.*, **185**(3), 1189–1219.
- Thunell, R., Tappa, E., Varela, R., Llano, M., Astor, Y., Muller-Karger, F. and Bohrer, R.** (1999) Increased marine sediment suspension and fluxes following an earthquake. *Nature*, **398**(6724), 233–236.
- Van Daele, M., Araya-Cornejo, C., Pille, T., Vanneste, K., Moernaut, J., Schmidt, S., Kempf, P., Meyer, I. and Cisternas, M.** (2019) Distinguishing intraplate from megathrust earthquakes using lacustrine turbidites. *Geology*, **47**, 127–130. <https://doi.org/10.1130/G45662.1>
- Van Daele, M., Meyer, I., Moernaut, J., De Decker, S., Verschuren, D. and De Batist, M.** (2017) A revised classification and terminology for stacked and amalgamated turbidites in environments dominated by (hemi)pelagic sedimentation. *Sed. Geol.*, **357**, 72–82.
- Van Daele, M., Moernaut, J., Doom, L., Boes, E., Fontijn, K., Heirman, K., Vandoorne, W., Hebbeln, D., Pino, M., Urrutia, R., Brümmer, R. and De Batist, M.** (2015) A comparison of the sedimentary records of the 1960 and 2010 great Chilean earthquakes in 17 lakes: Implications for quantitative lacustrine palaeoseismology. *Sedimentology*, **62**(5), 1466–1496.
- Vanneste, K., Wils, K. and Van Daele, M.** (2018) Probabilistic evaluation of fault sources based on paleoseismic evidence from mass-transport deposits: The example of aysén fjord, Chile. *J. Geophys. Res. Solid Earth.*, **123**(11), 9842–9865. <http://dx.doi.org/10.1029/2018jb016289>
- Vött, A., Hadler, H. and Koster, B.** (2018) Returning to the facts: Response to the refusal of tsunami traces in the ancient harbour of Lechaion (Gulf of Corinth, Greece) by “non-catastrophists”—Reaffirmed. *Zeitschrift Für Geomorphologie*, **61**(4), 275–302. <https://doi.org/10.1127/zfg/2018/0519>
- Watkins, S.E., Whittaker, A.C., Bell, R.E., McNeill, L.C., Gawthorpe, R.L., Brooke, S.A.S. and Nixon, C.W.** (2019). Are landscapes buffered to high-frequency climate change? A comparison of sediment fluxes and depositional volumes in the Corinth Rift, central Greece, over the past 130 k.y. *Geol. Soc. Am. Bull.*, **131**(3-4), 372–388.
- Wils, K., Deprez, M., Kissel, C., Vervoort, M., Van Daele, M., Daryono, M.R., Cnudde, V., Natawidjaja, D.H. and De Batist, M.** (2021) Earthquake doublet revealed by multiple pulses in lacustrine seismo-turbidites. *Geology*, **49**(11), 1301–1306.
- Zavala, C., Arcuri, M., Di Meglio, M., Diaz, H.G. and Contreras, C.** (2011). *A genetic facies tract for the analysis of sustained hyperpycnal flow deposits*. 31–51.
- Zavala, C. and Arcuri, M.** (2016) Intrabasinal and extrabasinal turbidites: Origin and distinctive characteristics. *Sed. Geol.*, **337**, 36–54.

*Manuscript received 10 March 2021; revision 24 November 2021; revision accepted 25 November 2021*

## Supporting Information

Additional information may be found in the online version of this article:

**Appendix S1.** Supplementary Fig. 1 shows Principal Component Analysis results of 24 selected XRF ratios (see *Methods*), whereas Supplementary Fig. 2 shows XRF counts of specific elements. Supplementary Figs 3 and 4 show XRF, grain-size/shape, magnetic and microtomography analyses of U-channels not presented in the main paper, and Supplementary Fig. 5 additional microtomographic images of U-Channels 2 and 8. Supplementary Fig. 6 gives all microtomographic images without any interpretation. Supplementary Table 1 gives an overview of observations and interpretations of the sedimentary events in all U-channels.